



AMERICAN METEOROLOGICAL SOCIETY

Journal of Climate

EARLY ONLINE RELEASE

This is a preliminary PDF of the author-produced manuscript that has been peer-reviewed and accepted for publication. Since it is being posted so soon after acceptance, it has not yet been copyedited, formatted, or processed by AMS Publications. This preliminary version of the manuscript may be downloaded, distributed, and cited, but please be aware that there will be visual differences and possibly some content differences between this version and the final published version.

The DOI for this manuscript is doi: 10.1175/JCLI-D-14-00634.1

The final published version of this manuscript will replace the preliminary version at the above DOI once it is available.

If you would like to cite this EOR in a separate work, please use the following full citation:

Coats, S., B. Cook, J. Smerdon, and R. Seager, 2014: North American Pan-Continental Drought in Model Simulations of the Last Millennium. *J. Climate*. doi:10.1175/JCLI-D-14-00634.1, in press.



1 **North American Pan-Continental Droughts in Model Simulations of the Last**

2 **Millennium**

3 Sloan Coats

4 *Lamont-Doherty Earth Observatory, Columbia University, Palisades, and Department*
5 *of Earth and Environmental Science, Columbia University, New York, New York*

6 Benjamin I. Cook

7 *NASA Goddard Institute for Space Studies, New York, and Lamont-Doherty Earth*
8 *Observatory, Columbia University, Palisades, New York*

9 Jason E. Smerdon

10 *Lamont-Doherty Earth Observatory, Columbia University, Palisades, New York*

11 Richard Seager

12 *Lamont-Doherty Earth Observatory, Columbia University, Palisades, New York*

13

14

15

16

17

18

19

20

21

22

23

24 Corresponding author address: Sloan Coats, Lamont-Doherty

25 Earth Observatory, 61 Route 9W, Palisades, NY 10964.

26 E-mail: sjc2164@columbia.edu

27 **Abstract:** Pan-continental droughts in North America, or droughts that
28 simultaneously affect a large percentage of the geographically and climatically
29 distinct regions of the continent, present significant on-the-ground management
30 challenges and, as such, are an important target for scientific research. The
31 methodology of paleoclimate-model data comparisons is used herein to provide a
32 more comprehensive understanding of pan-continental drought dynamics. Models
33 are found to simulate pan-continental drought with the frequency and spatial
34 patterns exhibited by the paleoclimate record. They do not, however, agree on the
35 modes of atmosphere-ocean variability that produce pan-continental droughts
36 because simulated El Niño-Southern Oscillation (ENSO), Pacific Decadal Oscillation
37 (PDO) and Atlantic Multidecadal Oscillation (AMO) dynamics, and their
38 teleconnections to North America, are different between models and observations.
39 Despite these dynamical differences, models are able to reproduce large-magnitude
40 centennial-scale variability in the frequency of pan-continental drought
41 occurrence—an important feature of the paleoclimate record. These changes do not
42 appear to be tied to exogenous forcings, suggesting that simulated internal
43 hydroclimate variability on these timescales is large in magnitude. Results both
44 clarify understanding of the dynamics that produce real-world pan-continental
45 droughts, while assessing the ability of models to accurately characterize future
46 drought risks.

47

48

49

50 **1. Introduction**

51 North America spans three countries, nearly 10 million square miles and
52 multiple geographical regions with distinct climates, seasonalities, and connections
53 to the wider atmosphere-land-ocean system. While each of the distinct geographic
54 and climatic regions in North America (e.g. the Southwest—32°–40°N, 125°–
55 105°W—versus the Central Plains—34°–46°N, 102°–92°W) experience recurrent
56 drought (e.g. Cook et al. 2007; McCabe et al. 2004; Nigam et al. 2011; Schubert et al.
57 2004a,b; Seager et al. 2005; Seager and Hoerling 2014), drought simultaneously
58 affecting multiple regions (hereinafter pan-continental drought) has also been
59 shown to be a consistent, albeit infrequent occurrence over the last millennium
60 (Cook et al. 2014a). The most recent pan-continental drought event occurred in
61 2012 (Hoerling et al. 2014) with 62% of the contiguous United States being
62 classified as moderately or extremely dry (NCDC 2013a). Events such as these pose
63 significant management challenges because of the simultaneous drought impacts
64 across regions with distinct water resource constraints (e.g., irrigation from rivers
65 versus groundwater), ecosystems (e.g., forests and grasslands), and crops.
66 Understanding the dynamics that drive pan-continental drought is therefore critical,
67 but there are two fundamental reasons why a comprehensive characterization of
68 pan-continental droughts, and their causes, proves challenging: 1) Regional
69 hydroclimate is characterized by distinct atmosphere-ocean dynamics—for instance
70 Southwestern hydroclimate is controlled primarily by winter precipitation
71 variability coupled to the tropical Pacific (e.g. Herweijer et al. 2006; Seager et al.
72 2008; Schubert et al. 2009), while the Great Plains has predominantly summer

73 hydroclimate variability that is driven by the tropical and subtropical Atlantic (e.g.
74 Sutton and Hodson 2005; Kushnir et al. 2010) in addition to the tropical Pacific
75 (Seager et al. 2005); 2) The relative rarity of pan-continental drought and the short
76 (~150 year) observational record means that there are few events by which to
77 diagnose how relatively distinct regional hydroclimate dynamics can combine to
78 produce pan-continental drought. The limitations of the short observational record
79 were partially addressed by Cook et al. (2014a) who employ a tree-ring based
80 reconstruction of North American hydroclimate over the last millennium (the North
81 American Drought Atlas or NADA—Cook et al. 2007) to better characterize the
82 statistics of pan-continental drought occurrence. The paleoclimate record, however,
83 does not provide a complete picture of the atmosphere-ocean state during pan-
84 continental droughts. Extending the analyses of Cook et al. (2014a) to the model
85 space using the methodology of paleoclimate-model data comparisons (e.g.
86 Anchukaitis et al. 2012; Ault et al. 2013, 2014; Coats et al. 2013a, 2014; Fernández-
87 Donado et al. 2012; Phipps et al. 2013; Schmidt et al. 2013) can provide additional
88 characterizations of past pan-continental droughts (albeit with the caveat of model
89 bias) and potentially help clarify our understanding of the dynamics that produce
90 these features. Additionally, the frequency of pan-continental drought occurrence is
91 likely to increase in the future as much of North America is expected to dry over the
92 coming century (e.g. Seager et al. 2013; Cook et al. 2014b; Maloney et al. 2014).
93 Because atmosphere-ocean general circulation models (AOGCMs) are used to make
94 these future hydroclimate projections, determining if AOCCMs are capable of
95 reproducing the statistics of past pan-continental drought occurrence, and as a

96 consequence of the correct dynamical drivers, is necessary to assess whether state-
97 of-the-art AOGCMs can accurately constrain future drought risks.

98 We build off the proxy analyses of Cook et al. (2014a) by employing coupled
99 model simulations to further assess the dynamics of pan-continental drought in
100 North America. We use the same gridded tree-ring based reconstruction of
101 hydroclimate variability (Cook et al. 2007) over North America from 1000-2005 C.E.
102 used by Cook et al. (2014a) and compare it to pan-continental drought statistics and
103 dynamics in forced transient simulations of the last millennium (850-1850 C.E.) and
104 the historical interval (1850-2005 C.E.), and in 500-year control simulations from
105 the same models—all from the Coupled and Paleo Model Intercomparison Projects
106 Phases 5 and 3 (CMIP5/PMIP3—Taylor et al. 2012; Schmidt et al. 2011). Four
107 fundamental questions are addressed:

108 1) Do models simulate the major modes of atmosphere-ocean variability that
109 impact North American hydroclimate (Section 3a)?

110 2) Are models able to reproduce the statistics of pan-continental drought
111 occurrence (Section 3b)?

112 3) Do the models have centennial-scale variability in the occurrence of pan-
113 continental droughts, and if so, is this driven by forced or internal variability
114 (Section 3c)?

115 4) What are the simulated atmosphere-ocean dynamics that drive pan-
116 continental droughts (Section 3d)?

117 **2. Data and Methods**

118 *a. Model and Paleoclimate Inputs*

119 All employed model output is from the CMIP5/PMIP3 archive (Table 1). We
120 use six Last Millennium (LM) simulations spanning the period 850-1850 C.E. that
121 are forced with reconstructed time varying exogenous forcings (Schmidt et al.
122 2011). These simulations have been appended to CMIP5 historical runs that span
123 the period 1850-2005 C.E. to produce a model record from 850-2005 C.E. Although
124 these simulations are not continuous, both of the paired simulations (historical and
125 LM) have been generated using the same model configurations and resolutions.
126 Consequently, if the simulations have no drift, the discontinuity at 1850 should fall
127 within the range of simulated climate variability. A large temperature drift in the
128 MIROC LM simulation (Sueyoshi et al. 2012) likely violates this assumption, while a
129 drift in the early centuries of the GISS LM simulation (Bothe et al. 2013) is likely to
130 have less of an impact. While model drift undoubtedly impacts the hydroclimate
131 variables assessed in this study, the effects are presumed to be moderate given the
132 absence of drift in precipitation (Sen Gupta et al. 2013). 500-year control
133 simulations with constant preindustrial forcings (also from CMIP5) were
134 additionally analyzed to aid in the interpretation of the LM model results. All model
135 output has been regridded to a common $2.5^{\circ} \times 2.5^{\circ}$ latitude-longitude grid to allow
136 for homogenous comparisons (this represents a coarsening of the model resolution
137 for 4 out of 6 models).

138 For each model simulation we calculate the Palmer Drought Severity Index
139 (PDSI—Palmer 1965). PDSI is an offline estimate of soil moisture balance, and has
140 been established as a robust estimator of soil moisture variability that compares
141 well with other soil moisture metrics (e.g. the Standardized Precipitation

142 Evapotranspiration Index—SPEI; Vicente Serrano et al. 2010; Cook et al. 2014b) and
143 inherent model soil moisture (Cook et al. 2014b; Smerdon et al. 2014). PDSI is
144 calculated from supply via precipitation and losses due to evapotranspiration (ET).
145 In this case, ET is calculated by means of scaling potential evapotranspiration (PET),
146 estimated from surface net radiation (RNET), by a fixed beta function meant to
147 represent vegetative controls on transpiration. There are multiple ways to compute
148 PET with the ideal method being Penman-Monteith (PM), which includes the effect
149 of the vapor pressure deficit along with the impact of RNET (a more detailed
150 treatment of PM PDSI can be found in Sheffield et al. 2012; Cook et al. 2014;
151 Smerdon et al. 2014). The necessary model fields to compute PM PET were only
152 available for three out of the six analyzed LM simulations and as a consequence
153 RNET instead has been used to calculate PET by assuming that RNET is exactly
154 balanced by latent heat through ET (with sensible heat flux equal to zero).
155 Importantly, PDSI calculated with PET estimated from RNET compares well with PM
156 PDSI on both interannual and decadal timescales (Coats et al. 2014).

157 For the analyses herein, model PDSI is derived on an even 2.5°x2.5° latitude-
158 longitude grid. At each grid point PDSI was calculated and then standardized against
159 an instrumental normalization period (1931-1990 C.E.) for the forced simulations,
160 and the full 500-year period for the control simulations. The instrumental
161 normalization period is the same time interval used by the National Oceanographic
162 and Atmospheric Administration for normalization of their PDSI calculations, which
163 were subsequently used as the target PDSI for the paleoclimate reconstructions
164 described below. Soil moisture capacity was specified as 25.4 mm and 127 mm in

165 the top and bottom layers of the PDSI calculation, respectively. The PDSI was
166 averaged over June-July-August (JJA) to produce a single average for each year;
167 hereinafter any mention of PDSI will be with regard to the JJA average values. PDSI
168 with an absolute value greater than ten was removed by replacement with the
169 average PDSI of the 8 neighboring grid points at that time step as a means of
170 removing unrealistically anomalous PDSI values. This method for removing data
171 errors is consistent with that used by van der Schrier et al. (2011) in the calculation
172 of their observed PDSI dataset. For a more detailed analysis of the PDSI data used
173 herein see Coats et al. (2014). Additionally, for a full treatment of the impact of
174 inherent model resolution on the simulation of hydroclimate over the study region
175 see Sheffield et al. (2013) and Langford et al. (2014), and for a discussion of how
176 these resolution biases may impact the PDSI data described above, and used herein,
177 see Coats et al. (2014).

178 Reconstructed PDSI data are from an updated version of the tree-ring
179 derived North American Drought Atlas (NADA) version 2a, with improved spatial
180 coverage and resolution, the full details of which can be found in Cook et al. (2014a).
181 The data are reconstructed on a $0.5^{\circ} \times 0.5^{\circ}$ latitude-longitude grid of JJA average PDSI
182 values for the United States, as well as parts of Canada and Northern Mexico.

183 Observed monthly PDSI data are from a global dataset for the period 1870-
184 2012 C.E. (Dai et al. 2004). This data was derived on an even $2.5^{\circ} \times 2.5^{\circ}$ latitude-
185 longitude grid using observed precipitation and temperature data as inputs. For the
186 analyses herein the JJA monthly PDSI values have been averaged to create a single
187 PDSI anomaly for each year. Additionally, only the period after 1950 will be

188 employed herein, as this is the period over which the full North American PDSI grid
189 is available.

190 JJA PDSI reflects hydroclimate conditions for the past 12-18 months because
191 of persistence built into the PDSI calculation, and as a consequence, will integrate
192 both the winter and summer hydroclimate state in any given year. Nevertheless,
193 tree-ring reconstructed PDSI has been shown to predominately reflect winter
194 season precipitation variability over the western United States, and both winter and
195 summer precipitation variability over the central and eastern United States (St.
196 George et al. 2011), a characteristic that may be shared by the models. Given
197 uncertainty with respect to the seasonal hydroclimate influences on PDSI, no
198 attempt is made herein to analyze the seasonality of pan-continental drought
199 dynamics.

200 *b. Climate Indices*

201 All climate indices are calculated using either the inherent surface
202 temperature output from the control simulations or observations from the National
203 Oceanic and Atmospheric Administration (NOAA) extended reconstructed sea
204 surface temperature (SST) dataset (Smith and Reynolds 2003). The Niño3.4 index
205 was calculated by averaging December-January-February (DJF) SST over the region
206 170°W-120°W, 5°S-5°N. The Pacific Decadal Oscillation (PDO) was evaluated by
207 calculating the EOFs of SST over the extra-tropical Pacific basin (60°W-75°E, 20°N-
208 90°N), and subsequently using the DJF average of the principle component
209 timeseries corresponding to the EOF that best matches the first EOF of the observed
210 record (which is defined as the observed PDO following Mantua et al. 1997) when

211 comparing the EOF patterns over the full (Northern and Southern Hemisphere)
212 Pacific basin. This was the first EOF for all models except BCC, in which the second
213 EOF was more representative of the observed PDO pattern. In all cases the model
214 patterns exhibit hemispheric symmetry and a tropical expression, as is
215 characteristic of the observed PDO. The Atlantic Multidecadal Oscillation (AMO) was
216 calculated by averaging JJA Atlantic SSTs over the region 80°W-0°E, 0°N-60°N and
217 then subtracting the global JJA SST average between 60°S-60°N (following Enfield et
218 al. 2001). All correlations between simulated PDSI and climate indices will be
219 calculated using the JJA grid point PDSI and either the preceding DJF average ENSO
220 or PDO indices or the contemporaneous JJA average AMO index.

221 *c. Analysis*

222 Following Cook et al. (2014a) the regional boundaries used in this paper are
223 the Southwest (SW): 32°N-40°N, 125°W-105°W; Central Plains (CP): 34°N -46°N,
224 102°W-92°W; Northwest (NW): 42°N-50°N, 125°W-110°W; and Southeast (SE):
225 30°N-39°N, 92°W-75°W (see regions in Figure 1). Similar to results shown for the
226 NADA in Cook et al. (2014a), the designated regions in the models do not have
227 climate variability that is completely independent. Nevertheless, correlation maps
228 between the four regional-average time series and grid-point PDSI indicate that
229 hydroclimate within each region is homogenous, and that variability between
230 individual regions is largely independent (not shown).

231 Again following Cook et al. (2014a), droughts are characterized to have
232 occurred in the regional-mean time series when PDSI falls to a value of -0.5 or lower
233 in any individual year. Pan-continental droughts are then defined as occurring when

234 any three [SW, CP, and SE (hereafter, SW+CP+SE); SW, CP, and NW (hereafter,
235 SW+CP+NW); SW, NW, and SE (hereafter, SW+NW+SE); or CP, NW, and SE
236 (hereafter, CP+NW+SE)] or all four [SW, CP, NW, and SE (hereafter,
237 SW+CP+NW+SE)] of the regional mean timeseries simultaneously have PDSI values
238 of -0.5 or lower in the same year. By this definition, the four-region droughts will
239 overlap with, and also be counted as, three-region droughts. For some of the
240 analyses noted in the results section the three- and four-region droughts were
241 treated as distinct events.

242 To determine the significance of the pan-continental drought teleconnections
243 (Niño3.4, PDO, and AMO), climate index composites are computed for all years that
244 exhibit pan-continental drought. A 5000-member ensemble resampling of the
245 climate indices is then performed to generate 90th percentile confidence limits. For
246 example, for the full CCSM control simulation there are 83 years that qualify as
247 SW+CP+SE droughts. An average of the Niño3.4 values for these 83 years gives a
248 composite Niño3.4 anomaly associated with these events. We then draw 83 random
249 years from the Niño3.4 time series and average them, repeating this process 5000
250 times. If the original composited Niño3.4 anomaly exceeds the 90th percentile
251 thresholds of the ensemble resampling, the association between pan-continental
252 drought and the dynamic teleconnection is characterized as significant.

253 **3. Results and Discussion**

254 *a. Model Dynamics*

255 To diagnose the dynamical drivers of pan-continental drought, the Niño3.4,
256 PDO and AMO indices are used to assess the relationships between pan-continental

257 drought and the major modes of atmosphere-ocean variability that impact North
258 American hydroclimate. In this section, we investigate the model expression of the
259 ENSO, PDO and AMO to determine if the simulated modes of variability are a
260 reasonable representation of real-world dynamics. For ENSO, negative values of the
261 Niño3.4 index, or La Niña conditions, have been associated with drought in the SW,
262 southern CP, and the SE. The PDO may not be fully separable from ENSO—the two
263 modes of variability are negatively correlated (Newman et al. 2003) and therefore
264 have similar spatial expressions. Nevertheless, the PDO has been shown to have
265 important hydroclimate impacts over North America (e.g., McCabe and Dettinger
266 2002; McCabe et al. 2004, 2008). A positive AMO, with warm Atlantic SSTs is
267 associated with drying in the CP and SE (Kushnir et al. 2010; McCabe et al. 2004,
268 2008; Nigam et al. 2011), and unlike the ENSO and PDO has considerable
269 persistence up to multi-decadal timescales.

270 Figure 1 shows the teleconnection patterns calculated as the correlation
271 between the Niño3.4, PDO and AMO indices and PDSI over North America. These
272 patterns have been calculated for both the NADA and an observed PDSI dataset (DAI
273 et al. 2004) during the overlapping period with the observed SST data set (1854-
274 2005 C.E. and 1950-2005 C.E., respectively), and for a sliding 152-year window (the
275 length of the observed/reconstruction overlap) across the full control model
276 simulations. The model pattern in Figure 1 plots the 152-year period in which the
277 simulated teleconnection pattern best represents the pattern between the observed
278 SST dataset and the reconstruction (hereafter observation-to-reconstruction), as
279 determined by the maximum centered pattern correlation statistic (hereinafter

280 CPCS—Santer et al. 1995) between the two fields. The CPCS is a quantitative
281 measure of the similarity of the simulated and observation-to-reconstruction
282 teleconnection patterns, with the range in the CPCS for all of the 152-year periods in
283 the models being a measure of the stationarity of that simulated teleconnection (the
284 middle panel of Figure 1). Additionally, the bottom panel of Figure 1 shows the
285 strength of the ENSO, PDO and AMO teleconnections. To do so, the sum of the
286 squared teleconnection correlation coefficients was calculated for each of the model
287 segments and the range in these values was then plotted as a boxplot. For
288 comparison, the sum of squared teleconnection correlation coefficients was also
289 calculated for the full observation-to-reconstruction and observational records. This
290 analysis was limited to the grid-points common to each dataset over the plotted
291 North American domain in the top panels of Figure 1.

292 The reconstruction-to-observation ENSO and AMO dynamics are largely
293 characteristic of those in the observed PDSI dataset with CPCS values between the
294 patterns of 0.75 and 0.50 and nearly equal strengths. The PDO teleconnection,
295 however, is significantly weaker in the reconstruction, despite having a similar
296 spatial pattern (CPCS of 0.52). While this may suggest a deficiency in the
297 reconstruction, it is more likely indicative of an inconsistent impact of the PDO over
298 the much longer reconstructed record (152 versus 56 years for the observed PDSI).

299 The models are able to simulate 152-year periods that have a realistic ENSO
300 teleconnection pattern to North America (with the exception of BCC), however the
301 strength of this teleconnection varies greatly with CCSM having far too strong of a
302 teleconnection and BCC and GISS having an ENSO teleconnection that is too weak.

303 The stationarity of this teleconnection, likewise, varies significantly between the
304 models; the CCSM ENSO teleconnection, for instance, is highly stationary while the
305 ENSO teleconnections in BCC and MIROC are highly non-stationary. The AMO and
306 PDO teleconnections in the models are much less realistic, with none of the models
307 simulating a 152-year period with a CPCS value over 0.6 and the teleconnection
308 strength being weaker than the observations for each model and both modes. These
309 teleconnections are also non-stationary, with the largest CPCS range occurring in
310 MIROC for the PDO and BCC for the AMO, but with a CPCS range of at least 0.4 for all
311 of the models.

312 Figures 2-4 show the SST spatial pattern and autocorrelation of the ENSO,
313 PDO and AMO for the full model simulations and observations. To assess the model
314 skill in reproducing the observed ENSO, PDO and AMO spatial patterns, Figure 5
315 shows the range in the CPCS between simulated spatial patterns calculated for a
316 sliding 152-year window (length of the observed SST dataset) across the full control
317 model simulations and the observed spatial patterns. Finally, Figure 6 shows the
318 variance of, or variance explained, by these dynamic modes. As suggested by the
319 teleconnections, models are generally successful at simulating a reasonable ENSO
320 spatial pattern (with the highest pattern correlation values of the three modes—
321 Figure 5), although the SST anomalies extend too far West in all of the models
322 (Figure 2). Additionally, the simulated ENSO autocorrelation structures are largely
323 characteristic of the observations, with oscillatory behavior that varies between
324 negative and positive. This oscillation looks to be most realistic in CCSM, IPSL and
325 MPI, with a cycle of variability that is too short and regular in BCC and GISS. The

326 magnitude of ENSO variability is not consistent across the models, with CCSM
327 having too much variance, while GISS, IPSL and MIROC have too little, as compared
328 to the observations (Figure 6). Interestingly, the simulated PDO and AMO behavior
329 is largely consistent between the models with a highly non-stationary, but at times
330 realistic PDO pattern (every model simulates a PDO pattern CPCS of at least 0.6),
331 and a more stationary, but generally unrealistic, AMO pattern (Figure 5). In both
332 cases, however, the PDO and AMO patterns in the models are less characteristic of
333 the observed patterns than for ENSO. Additionally, the BCC and GISS models fail at
334 simulating the magnitude of the observed tropical expression of the PDO, with all of
335 the models overestimating the high latitude North Pacific expression of the PDO
336 relative to the expression in the tropics. This is critical because the PDO forcing of
337 hydroclimate variability has been shown to originate in the tropical Pacific (Seager
338 2014).

339 The persistence characteristics of the PDO and AMO are plotted for both the
340 forced and control simulations in the right hand panels of Figures 3 and 4,
341 respectively. While the models have a reasonable PDO autocorrelation structure
342 (with the exception of BCC and the forced GISS and IPSL simulations—each having
343 too much persistence), with the exception of CCSM and GISS they struggle at
344 simulating the AMO with enough persistence (this is consistent with the behavior of
345 the CMIP3 model ensemble (Ting et al. 2011)). This lack of persistence suggests that
346 models will have difficulty in simulating the observed drought recurrence interval
347 (or alternatively drought persistence) in the CP and SE regions, which are tightly
348 coupled to the AMO in the real world (Kushnir et al. 2010; McCabe et al. 2004, 2008;

349 Nigam et al. 2011; and Ting et al. 2011). Finally, the magnitude of the PDO and AMO
350 will partially determine the impact of these modes of variability, relative to the
351 impact of ENSO and purely atmospheric variability, on North American
352 hydroclimate. There is a large inter-model spread in the variance or variance
353 explained by both modes, with CCSM and MIROC having too much and BCC, GISS,
354 IPSL and MPI having too little PDO variability compared to observations, and BCC,
355 CCSM, GISS and MPI having less AMO variability than observed (Figure 6).

356 In aggregate, the models exhibit different teleconnections between the
357 oceanic boundary conditions and North America, with no individual model matching
358 the observed atmosphere-ocean dynamics particularly well. Together, this suggests
359 that models are not likely to agree on the modes of atmosphere-ocean variability
360 that are associated with pan-continental drought. Additionally, the models have a
361 stronger and more realistic ENSO and associated teleconnections, as compared to
362 the PDO and AMO and are therefore expected to be more successful at simulating
363 the pan-continental drought dynamics associated with this mode of variability.
364 Nevertheless, the simulated dynamical relationships are largely non-stationary, and
365 the observed dynamics have been inferred from the short 152-year instrumental
366 interval. The observed dynamics, thus, may themselves be time variable or
367 inadequately characterized (particularly given the large persistence and
368 consequently the small number of degrees of freedom for the PDO and AMO). It is
369 therefore difficult to attribute differences between the models and observations as
370 solely associated with the model characteristics, as opposed to some combination of

371 model misrepresentations and poorly characterized observational teleconnections
372 due to undersampling of low-frequency modes and non-stationarity.

373 *b. Pan-Continental Drought Occurrence*

374 Figure 7 shows the drought recurrence interval for the individual geographic
375 regions in both forced and control simulations from the models (dark and light bars,
376 respectively) and the NADA. Models, in general, are able to simulate the correct
377 recurrence interval for drought in each of the regions. The model ensemble,
378 however, slightly overestimates the occurrence of SW and NW drought, and
379 underestimates the occurrence of drought in the CP and SE. This model behavior
380 may be suggestive of more realistic, and in some cases overactive, ENSO variability
381 and teleconnections (e.g. CCSM) relative to other modes of coupled atmosphere-
382 ocean variability, because ENSO driven hydroclimate variability tends to load
383 heavily on the western United States and thus predominantly affects the SW and NW
384 regions.

385 The model ensemble is also largely successful at simulating the pan-
386 continental drought recurrence intervals characterized by the NADA (again for both
387 forced and control simulations—Figure 8). Taken individually, however, the models
388 appear split into two categories, with CCSM, IPSL, and MPI slightly underestimating
389 the recurrence interval of pan-continental drought of all types and GISS and MIROC
390 overestimating the recurrence interval of these droughts by a much larger margin
391 (BCC has realistic recurrence intervals for three of the five pan-continental drought
392 types). Nevertheless, the spread of the model ensemble encompasses the pan-
393 continental drought recurrence interval of the NADA for each drought type.

394 Furthermore, each model is individually successful at capturing the relative
395 occurrence of the different types of pan-continental drought, for instance the
396 SW+CP+SE combination being the most common and the SW+CP+NW+SE
397 combination being the least common.

398 The recurrence intervals for the droughts in the individual regions and for
399 pan-continental droughts are not consistently different for the forced and control
400 simulations (Figures 7 and 8). This suggests that the simulated pan-continental
401 drought dynamics are not dependent on the exogenous forcing and, as such,
402 provides confidence in the use of control simulations to assess simulated
403 atmosphere-ocean variability and its connection to pan-continental drought
404 (Sections 3a and 3d). These findings are consistent with previous work that has
405 specifically focused on the dynamics of persistent droughts in the Southwest (Coats
406 et al. 2013; 2014).

407 The composite PDSI pattern of each pan-continental drought type for the
408 control model simulations and reconstruction are plotted in Figure 9. The bottom
409 panel of Figure 9 shows the CPCS calculated between the composite PDSI pattern
410 from the NADA and each individual pattern of that pan-continental drought type.
411 The range in CPCS is thus a measure of the consistency of individual drought
412 patterns (small range being more consistent), with the average magnitude of the
413 CPCS values for each model being indicative of how well the model composite
414 matches the NADA composite. These values have been calculated separately for the
415 three- and four-region droughts (unlike in previous analyses). The composite model
416 patterns compare well with the NADA composite for all but the SW+NW+SE

417 droughts, which are the least common of the pan-continental drought types. The
418 CPCS range in the models and the NADA are likewise consistent for all but the
419 SW+NW+SE combination. Nevertheless, it is important to note that for all drought
420 types there is a large CPCS range in both the models and the NADA. This indicates
421 that individual pan-continental droughts can have different spatial patterns. Pan-
422 continental droughts driven by a consistent dynamical driver might be expected to
423 have a consistent pattern. If this is the case, the large CPCS range may then suggest
424 that multiple dynamical drivers are capable of producing each type of pan-
425 continental drought. Equally likely, however, is that pan continental droughts are
426 influenced not just by SST variations but also by internal atmospheric variability
427 that can create different spatial patterns, as was argued for the 2012 drought by
428 Hoerling et al. (2014). A third possibility is that a large CPCS range would also be
429 expected if pan-continental droughts were driven by consistent dynamical drivers
430 but with teleconnection dynamics that are variable through time. The question of
431 pan-continental drought dynamical drivers will be addressed in Section 3d.

432 *c. Centennial Variability in Pan-Continental Drought Occurrence*

433 Perhaps the starkest characteristic of the NADA drought record is the
434 centennial-scale variability in the number of pan-continental droughts, punctuated
435 by an increased rate of occurrence in the MCA relative to the LIA (Cook et al. 2014a).
436 The relative timing of hydroclimate change in the models—if such changes are
437 present in the CMIP5 models—and the NADA is of particular interest because
438 exogenous forcing may, or may not, have played a role in driving the MCA-to-LIA
439 transition (e.g. Mann et al. 2009; González-Ruoco et al. 2011; Goosse et al. 2012). If,

440 in fact, radiative forcing produced this transition it would be relevant to our
441 understanding of current and future radiatively forced climate change. Because the
442 models are driven with similar forcing series (see Schmidt et al. [2011]), a strong
443 role for exogenous forcing in driving periods with increased pan-continental
444 drought frequency should lead to these periods being contemporaneous in time
445 across the model simulations. The role of radiative forcing in driving variability of
446 pan-continental drought frequency on centennial timescales can therefore be tested
447 to potentially better understand the origin of this variability in the NADA. It must be
448 noted, however, that the CMIP5 models have different climate sensitivities, and in
449 particular, different parameterizations of land surface and aerosol processes that
450 may drive compensating feedbacks and mask the model response to external
451 forcing. If these differences are large it would impact our ability to test the
452 hypothesized role of forcing as posed above, a possibility that is outside the scope of
453 this paper.

454 The number of pan-continental droughts for each century relative to the
455 mean number of droughts per century between 1000-2000 C.E. is plotted for the
456 forced model simulations and the reconstruction in Figure 10. For the NADA, the
457 increase in the number of pan-continental droughts, relative to mean conditions,
458 during the 12th century averages to 60%, with a maximum increase of 75% for the
459 SW+CP+NW drought type and a minimum of 40% for the SW+NW+SE type. This
460 period of increased drought frequency does not appear to be captured by the
461 models, nor do the individual models agree on the timing of hydroclimate change,
462 suggesting that these changes are not tied in any coherent way to the exogenous

463 forcing. A possible exception is the CCSM model, which exhibits increased aridity
464 during the 11th-12th centuries (particularly manifest in the number of SW+CP+SE
465 drought occurrences, although the number of droughts in both centuries is within
466 the range from the CCSM control simulation)—changes that are contemporaneous
467 with those in the NADA. The models do, however, appear to simulate a large range
468 in the number of pan-continental droughts. To test if this range is of the magnitude
469 observed in the NADA, the number of each pan-continental drought type was
470 calculated for a sliding 100-year window across the forced model simulations and
471 NADA record and the range is plotted in Figure 11. Each model is individually
472 capable of simulating centennial-scale variability in the frequency of pan-
473 continental drought occurrence that is characteristic of the NADA. The fact that
474 models simulate large differences in the number of pan-continental drought
475 features for different 100-year periods, and that these changes are not tied in any
476 coherent way to the exogenous forcing, is suggestive of a large amount of internal
477 variability on centennial timescales. This model behavior is consistent with previous
478 work that has focused on dynamics of persistent drought in the Southwest
479 specifically (Coats et al. 2013; 2014). Additionally, if the model dynamics are in fact
480 representative of the real atmosphere-ocean system then this result indicates that
481 the observed preponderance of pan-continental droughts in the Medieval period
482 could have arisen from internal variability, as opposed to changes in radiative
483 forcing.

484 *d. Simulated Pan-Continental Drought Dynamics*

485 Figure 12 shows the composite of the Niño3.4, PDO and AMO indices during
486 each type of pan-continental drought for the model control simulations and for the
487 overlapping period between the NADA and the observed SST data set (1854-2005
488 C.E.), with this analysis completed separately for the three- and four-region
489 droughts. Significance at the 90% level using the bootstrapping test described in
490 Section 2c is indicated with an asterisk. Importantly, the models do not agree with
491 each other or the observations on the dynamics that drive the different types of pan-
492 continental drought, despite the fact that they produce patterns and recurrence
493 intervals that are consistent with the NADA (Figure 8-10). The one exception
494 appears to be the importance of ENSO to the SW+CP+SE, SW+CP+NW, SW+NW+SE
495 and SW+CP+NW+SE pan-continental drought types, which is exhibited to varying
496 degrees by all of the models and for the observation-to-reconstruction. Additionally,
497 with the exception of CCSM and MPI, the models and the observations individually
498 have pan-continental drought types with no significant connection to the major
499 modes of atmosphere-ocean variability. Together these results imply what was
500 suggested by the large CPCS range in the bottom panel of Figure 9 and by the
501 characteristic model behavior outlined in Section 3a, namely that multiple
502 dynamical drivers are capable of producing each type of pan-continental drought.

503 The left hand panel of Figure 13 shows the observed Niño3.4, PDO and AMO
504 indices with the timing of each pan-continental drought occurrence marked with a
505 grey bar. While the ENSO behavior appears to be consistent throughout the
506 instrumental interval, the variability in the early part of the PDO and AMO records is
507 subdued. This behavior may explain the weaker PDO and AMO teleconnections in

508 the reconstructed PDSI, relative to observations (bottom panel of Figure 1), as the
509 reconstruction spans the length of the 152-year instrumental SST record. The
510 observed PDSI, by contrast, is analyzed only over the 1950-2005 period for which
511 both modes exhibit consistently large variability.

512 The right hand panel of Figure 13 and Figure 14 analyze the associations
513 between pan-continental droughts and the dynamical drivers using the observation-
514 to-reconstruction and the models respectively, but allowing for a more robust
515 statistical assessment of the possibility that it is a combination of dynamical modes
516 that produces pan-continental drought features. To do so, all pan-continental
517 drought types are treated as the same, and considered as a Bernoulli process (with 1
518 for drought years and 0 for non-drought years), with the drought frequency then
519 defined as the number of pan-continental drought occurrences over the number of
520 analyzed years (152 for the observations/reconstruction and 500 years for the
521 model control simulations). Within a Bayesian framework, the posterior
522 distribution of the drought frequency can be calculated for subsets of the data that
523 have different phases of the dynamic modes (e.g. a negative or La Niña-like state in
524 the Niño3.4 index) or some combination of phases of the dynamic modes (e.g. a
525 negative Niño3.4 index, positive AMO, and negative PDO). If, following Kam et al.
526 (2014), we assume that the prior distribution is a uniform beta distribution or
527 uninformative, then the posterior distribution is easily derived with the alpha and
528 beta parameters being equal to the number of drought occurrences plus one and the
529 number of years minus the number of drought occurrences plus one, respectively.
530 The observation-to-reconstruction posterior distributions in the right hand panel of

531 Figure 13 indicate that the frequency of pan-continental drought occurrence is
532 greatest when there are simultaneously negative Niño3.4 and PDO indices and a
533 positive AMO index (with pan-continental drought occurring nearly 40% of the time
534 when these conditions are met). Interestingly, for the observation-to-reconstruction
535 the individual impact of the three modes of variability on the frequency of pan-
536 continental drought is roughly equal. The models, by contrast, tend to overestimate
537 the impact of ENSO on pan-continental drought occurrence (with the main
538 exception being BCC—Figure 14). This result is likely indicative of the more
539 realistic, and in some cases overactive, ENSO variability and teleconnections (e.g.
540 CCSM) relative to other modes of coupled atmosphere ocean variability.

541 The model split between slightly underestimating the recurrence interval of
542 pan-continental drought of all types (CCSM, IPSL and MPI) and moderately
543 overestimating the recurrence interval of these droughts (BCC, GISS and MIROC) in
544 Figure 8 can also be explained by the results in Figures 13 and 14. CCSM, IPSL and
545 MPI all overestimate the impact of ENSO on the frequency of pan-continental
546 drought occurrence and, as a consequence, produce more of these features than is
547 realistic (Figure 14). In CCSM this behavior appears to result from ENSO variability
548 that is too strong (Figure 1 and Figure 2), while in IPSL and MPI the ENSO variability
549 is more realistic (though slightly too strong) but the hydroclimate response to ENSO
550 is too homogenous over the North American continent (Figure 1). BCC, despite
551 underestimating the impact of ENSO on pan-continental drought occurrence, is able
552 to largely reproduce the impact of the AMO, while slightly overestimating the PDO
553 impact (Figure 1), and has a posterior distribution of ocean forced pan-continental

554 drought occurrence that is similar to the observations/reconstruction (Figure 14).
555 The same is true of GISS, which exhibits the most realistic impact (as compared to
556 the observations) of the three modes of atmosphere-ocean variability (and the
557 oceanic boundary conditions in general—Figure 14) on pan-continental drought
558 occurrence (although it slightly underestimates the AMO impact relative to the
559 PDO). The fact that GISS, and to a lesser degree BCC, underestimate the overall
560 occurrence of pan-continental drought (e.g. Figure 8), therefore, appears to be
561 related to the frequency with which the simulated ocean produces a simultaneously
562 positive AMO, negative PDO and negative ENSO. MIROC also underestimates the
563 frequency of pan-continental drought occurrence, and while it simulates a
564 reasonable impact of a negative Niño3.4 index on the frequency of pan-continental
565 drought occurrence, the PDO and AMO impacts are too weak (Figure 14).

566 It must be noted that between the short instrumental record, which limits
567 our knowledge of real-world pan-continental drought dynamics, and the general
568 lack of consistency in the significance of connections between the dynamical modes
569 and pan-continental drought events in both the models and the NADA, it is difficult
570 to make conclusions about the veracity of the simulated dynamics. Nevertheless,
571 attempting to understand the simulated pan-continental drought dynamics in the
572 context of the characteristic model behavior outlined in Section 3a may help
573 determine if models will be able to properly constrain the risk of future drought
574 over North America. In particular, the behavior of CCSM and BCC are an interesting
575 juxtaposition of pan-continental drought dynamics. CCSM has significant
576 connections between four of the pan-continental drought types and the tropical

577 Pacific (Figure 12), and in general greatly overestimates the impact of ENSO on pan-
578 continental drought occurrence (Figure 14). BCC, on the other hand, has no
579 significant connections between pan-continental drought and the tropical Pacific
580 (Figure 12), and generally underestimates the impact of ENSO on pan-continental
581 drought occurrence (Figure 14). This behavior can perhaps be understood in terms
582 of the model dynamics outlined in Section 3a. While BCC has a somewhat realistic
583 ENSO spatial pattern (Figure 5), and variability that is moderate (but too regular—
584 e.g. the large negative lag-1 autocorrelation value—Figure 2), the ENSO
585 teleconnection to North America is the least realistic, weakest and most non-
586 stationary of the models analyzed herein (Figure 1). By contrast, the PDO and AMO
587 teleconnections are more realistic, stronger (Figure 1) and consequently more
588 strongly connected to pan-continental drought (Figure 14). CCSM, on the other
589 hand, has a very realistic and stationary ENSO teleconnection (Figure 1), along with
590 ENSO variability and spatial patterns that are too strong (Figure 5 and Figure 6). As
591 a consequence, nearly all of the pan-continental drought types exhibit a connection
592 to the tropical Pacific. Interestingly, the PDO and AMO in CCSM are less realistic and
593 exhibit relatively large and small variability (Figure 5 and Figure 6), respectively,
594 yet both have a significant connection to three of the pan-continental drought types
595 (Figure 12).

596 The behavior of the other models is less clear but will be considered
597 separately for models with weak ENSO (GISS and MIROC) and strong ENSO (IPSL
598 and MPI) connections to pan-continental drought in Figure 14. For weak ENSO, GISS,
599 while only exhibiting a significant connection between ENSO and two of the pan-

600 continental drought types (Figure 12), largely captures the oceanic impact on the
601 frequency of pan-continental drought occurrence (Figure 14). This is surprising
602 given that the GISS model underestimates the overall frequency of pan-continental
603 drought occurrence and has generally weak ocean variability (e.g. Coats et al. 2014).
604 MIROC also has a weak connection between the tropical Pacific and pan-continental
605 droughts (with just the connection between SW+CP+SE and ENSO being significant
606 at the 90% level—Figure 12), and this is likely related to the highly non-stationary
607 and unrealistic ENSO teleconnection within the model (Figure 1).

608 MPI, like CCSM, has a strong connection between ENSO and pan-continental
609 droughts with all of the drought types exhibiting significance (Figure 12). While the
610 ENSO teleconnection in MPI is less realistic than in CCSM (Figure 1), the model also
611 exhibits relatively large magnitude tropical Pacific variability (Figure 6). IPSL, like
612 CCSM and MPI, overestimates the impact of ENSO on pan-continental drought
613 occurrence (Figure 14); it also exhibits a moderate connection between the
614 individual pan-continental drought types and ENSO, with the SW+CP+SE and
615 SW+CP+NW+SE being significant at the 90% level (Figure 12). The ENSO
616 teleconnection in IPSL is likewise moderately realistic, as well as highly stationary
617 and driven by moderate variability in the tropical Pacific (Figure 1 and Figure 6).

618 **4. Conclusions**

619 Simulated ENSO, PDO and AMO dynamics and their teleconnections to North
620 America, differ between models and in their comparisons to observations. As a
621 consequence, models do not agree on the modes of atmosphere-ocean variability
622 that are associated with pan-continental droughts. The models do, however,

623 simulate pan-continental droughts with the frequency and spatial patterns exhibited
624 by the NADA. Additionally, the models display centennial-scale variability in the
625 occurrence of pan-continental droughts that is similar to the magnitude observed in
626 the NADA. These changes do not appear to be tied to the exogenous forcing,
627 suggesting that simulated internal hydroclimate variability on these timescales is
628 large in magnitude.

629 These results have implications for efforts to project future hydroclimate
630 over North America and to understand past hydroclimate change. Firstly, if
631 centennial-scale internal variability is large in magnitude, the MCA-to-LIA transition
632 and other periods of past hydroclimate change may have resulted from internal
633 variability of the atmosphere-ocean system. If true, this would suggest that the
634 projection of certain characteristics of future hydroclimate are potentially
635 complicated in terms of the impact of trace gas concentrations. Nevertheless,
636 internal variability, if manifest in changes to the oceanic boundary conditions that in
637 turn drive hydroclimate change, may be predictable if interannual-to-multidecadal
638 modes of Pacific and Atlantic Ocean variability can be predicted. While operational
639 prediction of the tropical Pacific, for instance, has yet to exceed the seasonal
640 timescale (e.g. Barnston et al. 2012; Zhu et al. 2012), the slowly varying nature of
641 the PDO and AMO suggests that it is a potential target for predictability on decadal
642 timescales (e.g. Smith et al. 2012). In the context of the results presented herein,
643 PDO and AMO predictability would help constrain risk assessments of future pan-
644 continental drought occurrence, given that a negative PDO and a positive AMO are
645 associated with an increased frequency of pan-continental drought occurrence

646 (Figure 13). In particular, decadal AMO and PDO predictability along with seasonal
647 ENSO prediction has the potential to provide robust annual projections of the risk of
648 pan-continental drought occurrence.

649 Secondly, models reproduce the statistics of pan-continental drought
650 occurrence, but they do not agree on the dynamics that drive these features. The
651 ENSO (e.g. Clement et al. 1996) and AMO (e.g. Ting et al. 2009) both potentially
652 respond to radiative forcing. If these responses are large in magnitude, the
653 simulated hydroclimate change over North America will be different for each model.
654 In CCSM, for instance, a large forced response in the tropical Pacific would be
655 expected to drive large hydroclimate impacts over North America. The same change
656 in BCC, however, would yield smaller impacts. It is difficult to determine which of
657 these model responses is realistic, and by consequence, which model projection
658 should be considered the most accurate, because even in models that are successful
659 at simulating the observed atmosphere-ocean dynamics the dynamical relationships
660 are often non-stationary and their connection to radiative forcings are not well
661 constrained. This issue is compounded by the fact that the observed dynamics
662 themselves have been inferred from a 152-year instrumental interval that cannot
663 provide a full assessment of the stationarity of real world dynamics. Understanding
664 whether teleconnection non-stationarity is physically reasonable, and whether the
665 instrumental interval is sufficient to characterize the full range of real world
666 atmosphere ocean dynamics, is thus essential for constraining the risk of
667 hydroclimate change in North America. This will require, at a minimum, longer
668 records of proxy estimated SSTs (e.g. Emile-Geay et al. 2013 for the tropical Pacific)

669 and other regional records of hydroclimate variability over the last millennium (e.g.
670 Cook et al. 2010—for monsoon Asia).

671 A characterization of the full range of real world atmosphere-ocean
672 dynamics, and their connections to pan-continental droughts, will help determine
673 which models exhibit realistic dynamics and thus can be interpreted as projecting
674 the future hydroclimate of North America with some accuracy. We have
675 demonstrated that models simulate pan-continental droughts that are characteristic
676 of a paleoclimate estimate (in spatial character and frequency of occurrence), but
677 driven by different atmosphere-ocean dynamics, and that these models simulate a
678 large degree of variability in the occurrence of pan-continental droughts on
679 centennial timescales. These results, and further efforts to characterize relevant
680 model dynamics, will help clarify the interpretation of future hydroclimate
681 projections by providing, in particular, an understanding of the reasons for the
682 differences between model projections of hydroclimate responses to increased
683 greenhouse gas forcing. This understanding, in turn, will help determine what
684 information from the future projections is useful for planning adaptation and
685 management strategies for the impacts of climate change.

686 **Acknowledgements:** This work was supported by NOAA awards
687 NA100AR4310137 (Global Decadal Hydroclimate Variability and Change, GloDecH)
688 and NA110AR4310166 and NSF awards AGS-1243204 and AGS-1401400. We
689 acknowledge the World Climate Research Programme's Working Group on Coupled
690 Modelling, which is responsible for CMIP, and we thank the climate modeling groups
691 (listed in supplementary Table 1) for producing and making available their model

692 output. For CMIP the U.S. Department of Energy's Program for Climate Model
693 Diagnosis and Intercomparison provides coordinating support and led development
694 of software infrastructure in partnership with the Global Organization for Earth
695 System Science Portal. We also thank Haibo Liu and Naomi Henderson for their
696 considerable computational and data management support. LDEO contribution
697 XXXX.

References:

- Anchukaitis, K. J., P. Breitenmoser, K. R. Briffa, A. Buchwal, U. Büntgen, E. R. Cook, R. D. D'Arrigo, J. Esper, M. N. Evans, D. Frank, H. Grudd, B. E. Gunnarson, M. K. Hughes, A. V. Kirilyanov, C. Körner, P. J. Krusic, B. Luckman, T. M. Melvin, M. W. Salzer, A. V. Shashkin, C. Timmreck, E. A. Vaganov, and R. J. S. Wilson, 2012: Tree rings and volcanic cooling. *Nature Geosci*, 5, 836-837. doi: <http://dx.doi.org/10.1038/ngeo1645>.
- Ault, T. R., J. E. Cole, J. T. Overpeck, G. T. Pederson, S. St. George, B. Otto-Bliesner, C. A. Woodhouse, C. Deser, 2013: The continuum of hydroclimate variability in western North America during the last millennium. *J. Climate*, 26, 5863–5878. doi: <http://dx.doi.org/10.1175/JCLI-D-11-00732.1>.
- Ault, T. R., J. E. Cole, J. T. Overpeck, G. T. Pederson, and D. M. Meko, 2014: Assessing the risk of persistent drought using climate model simulations and paleoclimate data. *J. Climate*, in press. doi: <http://dx.doi.org/10.1175/JCLI-D-11-00732.1>.
- Barnston, Anthony G., Michael K. Tippett, Michelle L. L'Heureux, Shuhua Li, David G. DeWitt, 2012: Skill of Real-Time Seasonal ENSO Model Predictions during 2002–11: Is Our Capability Increasing?. *Bull. Amer. Meteor. Soc.*, 93, 631–651. doi: <http://dx.doi.org/10.1175/BAMS-D-11-00111.1>.
- Bothe, O., Annan, J. H. Jungclaus, and D. Zanchettin, 2013: Consistency of the multi-model CMIP5/PMIP3-past1000 ensemble. *Clim. Past Discuss.*, 9, 2471-2487, doi:10.5194/cp-9-2471-2013.
- Clement, A. C., R. Seager, M. A. Cane, and S. E. Zebiak, 1996: An ocean dynamical thermostat.

J. Climate, 9, 2190–2196.

Coats, S., J. E. Smerdon, R. Seager, B.I. Cook, and J.F. González-Rouco, 2013a: Megadroughts in southwest North America in millennium-length ECHO-G simulations and their comparison to proxy drought reconstructions. *J. Climate*, 26, 7635-7649.

Coats, S., J. E. Smerdon, B. I. Cook, and R. Seager (2014), Are simulated megadroughts in the North American Southwest Forced?, *J. Clim.*, in review.

Cook, B. I., J. E. Smerdon, R. Seager, E. R. Cook, 2014a: Pan-Continental Droughts in North America over the Last Millennium. *J. Climate*, **27**, 383–397. doi: <http://dx.doi.org/10.1175/JCLI-D-13-00100.1>.

Cook, B.I., J.E. Smerdon, R. Seager, and S. Coats, 2014b: Global warming and 21st century drying. *Clim. Dyn.*, doi:10.1007/s00382-014-2075-y.

Cook, E. R., R. Seager, M. A. Cane, and D. W. Stahle, 2007: North American drought: Reconstructions, causes, and consequences. *Earth Sci. Rev.*, 81 (1–2), 93–134.

Cook, E. R., K. J. Anchukaitis, B. M. Buckley, R. D. D'Arrigo, G. C. Jacoby, and W.E. Wright, 2010: Asian monsoon failure and megadrought during the last millennium. *Science*, 328, 486-489.

Dai, A., K. E. Trenberth, and T. Qian, 2004: A global data set of Palmer Drought Severity Index for 1870-2002: Relationship with soil moisture and effects of surface warming. *J. Hydrometeorology*, 5, 1117-1130.

Emile-Geay, J., K. M. Cobb, M. E. Mann, A. T. Wittenberg, 2013: Estimating central equatorial Pacific SST variability over the past millennium. Part II: Reconstructions and

implications. *J. Climate*, 26, 2329–2352. doi: <http://dx.doi.org/10.1175/JCLI-D-11-00511.1>.

Enfield, D. B., A. M. Mestas-Nuñez, and P.J. Trimble, 2001: The Atlantic multidecadal oscillation and its relation to rainfall and riverflows in the continental U.S.. *Geophys. Res. Lett.*, 28(10), 2077-2080.

Fernández-Donado, L., González-Rouco, J. F., Raible, C. C., Ammann, C. M., Barriopedro, D., García-Bustamante, E., Jungclauss, J. H., Lorenz, S. J., Luterbacher, J., Phipps, S. J., Servonnat, J., Swingedouw, D., Tett, S. F. B., Wagner, S., Yiou, P., and Zorita, E., 2012: Temperature response to external forcing in simulations and reconstructions of the last millennium. *Clim. Past Discuss.*, 8, 4003-4073. doi: 10.5194/cpd-8-4003-2012.

González-Rouco, F. J., *and coauthors*, 2011. Medieval Climate Anomaly to Little Ice Age transition as simulated by current climate models. *PAGES news* **19**, 7–11.

Goosse, H., E. Cresspin, S. Dubinkina, M.-F. Loutre, M. E. Mann, and co-authors, 2012: The role of forcing and internal dynamics in explaining the “medieval climate anomaly”. *Clim. Dyn.* **39**, 2847–2866. DOI: 10.1007/s00382-012-1297-0.

Herweijer, C., R. Seager, and E. R. Cook, 2006: North American droughts of the mid to late nineteenth century: a history, simulation and implication for Mediaeval drought. *Holocene*, 16(2), 159-171.

Hoerling, M., J. Eischeid, A. Kumar, R. Leung, A. Mariotti, K. Mo, S. Schubert and R. Seager, 2014: Causes and predictability of the 2012 great plains drought. *Bulletin of the American Meteorological Society*, 269-282.

- Kam, J., J. Sheffield and E. F. Wood, 2014: Changes in drought risk over the contiguous United States (1901-2012): The influence of the Pacific and Atlantic Oceans. *Geophysical Research Letters*, in press.
- Kushnir, Y., R. Seager, M. Ting, N. Naik(Henderson) and J. Nakamura, 2010: Mechanisms of Tropical Atlantic SST Influence on North American Precipitation Variability. *J. Climate*, 23. doi: 10.1175/2010JCLI3172.1.
- Maloney, E. D., S. J. Camargo, E. Chang, B. Colle, R. Fu, K. L. Geil, Q. Hu, X. Jiang, N. Johnson, K. B. Karnauskas, J. Kinter, B. Kirtman, S. Kumar, B. Langenbrunner, K. Lombardo, L. N. Long, A. Mariotti, J. E. Meyerson, K. C. Mo, J. D. Neelin, Z. Pan, R. Seager, Y. Serra, A. Seth, J. Sheffield, J. Stroeve, J. Thibeault, S.-P. Xie, C. Wang, B. Wyman, and M. Zhao, 2014: North American climate in CMIP5 experiments: Part III: Assessment of 21st century projections. *J. Climate*, 27, 2230-2270.
- Mann, M. E., Z. Zhang, S. Rutherford, R. S. Bradley, M. K. Hughes, D. Shindell, C. Ammann, G. Faluvegi, and F. Ni, 2009: Global signatures and dynamical origins of the Little Ice Age and Medieval Climate Anomaly. *Science*, 27, 1256-1260.
- Mantua, N.J. and S.R. Hare, Y. Zhang, J.M. Wallace, and R.C. Francis, 1997: A Pacific interdecadal climate oscillation with impacts on salmon production. *Bulletin of the American Meteorological Society*, 78, 1069-1079.
- McCabe, G. J., and M. D. Dettinger, 2002: Primary modes and predictability of year-to-year snowpack variations in the western United States from teleconnections with Pacific Ocean climate. *J. Hydrometeor.*, 3, 13-25.
- McCabe, G. J., M. A. Palecki, and J. L. Betancourt, 2004: Pacific and Atlantic ocean influences

on multidecadal drought frequency in the United States. *Proc. Natl. Acad. Sci. USA*, 101, 12, 4136-4141.

McCabe, G.J., J. L. Betancourt, S. T. Gray, M. A. Palecki, and H. G. Hidalgo, 2008: Associations of multi-decadal sea-surface temperature variability with US drought. *Quat. Int.*, 188, 31–40. doi:10.1016/j.quaint.2007.07.001.

NCDC, cited 2013a: State of the climate: Drought–annual 2012. National Oceanic and Atmospheric Administration. [Available online at [http://www.ncdc.noaa.gov/sotc/drought/.](http://www.ncdc.noaa.gov/sotc/drought/)]

Newman, M., G. P. Compo, and M. A. Alexander, 2003: ENSO- forced variability of the Pacific decadal oscillation. *J. Climate*, 16, 3853–3857.

Nigam, S., B. Guan, and A. Ruiz-Barradas, 2011: Key role of the Atlantic Multidecadal Oscillation in 20th century drought and wet periods over the Great Plains, *Geophys. Res. Lett.*, 38, L16713, doi:10.1029/2011GL048650.

Phipps, S. J., and Coauthors, 2013: Paleoclimate Data–Model Comparison and the Role of Climate Forcings over the Past 1500 Years. *J. Climate*, **26**, 6915–6936. doi: <http://dx.doi.org/10.1175/JCLI-D-12-00108.1>.

Santer, B. D., K. E. Taylor, T. M. L. Wigley, J. E. Penner, P. D. Jones and U. Cubasch, 1995. Towards the detection and attribution of an anthropogenic effect on climate. *Climate Dynamics*, 12, 77-100.

Schmidt, G. A., J. H. Jungclaus, C. M. Ammann, E. Bard, P. Braconnot, T. J. Crowley, G. Delaygue, F. Joos, N. A. Krivova, R. Muscheler, B. L. Otto-Bliesner, J. Pongratz, D. T. Shindell, S. K. Solanki, F. Steinhilber, and L. E. A. Vieira, 2011: Climate forcing

reconstructions for use in PMIP simulations of the last millennium (v1.0). *Geosci. Model Dev.*, 4, 33-45, doi:10.5194/gmd-4-33-2011.

Schmidt, G. A., J. D. Annan, P. J. Bartlein, B. I. Cook, E. Guilyardi, J. C. Hargreaves, S. P. Harrison, M. Kageyama, A. N. LeGrande, B. Konecky, S. Lovejoy, M. E. Mann, V. Masson-Delmotte, C. Risi, D. Thompson, A. Timmermann, L.-B. Tremblay, and P. Yiou, 2013: Using paleo-climate comparisons to constrain future projections in CMIP5. *Clim. Past Discuss.*, 9, 775-835, doi:10.5194/cpd-9-775-2013.

Schubert, S. D., M. J. Suarez, P. J. Pegion, R. D. Koster, and J. Bacmeister, 2004a: Causes of long-term drought in the US Great Plains. *J. Climate*, 17(3), 485-503.

Schubert, S. D., M. J. Suarez, P. J. Pegion, R. D. Koster, and J. Bacmeister, 2004b: On the cause of the 1930s Dust Bowl. *Science*, 303(5665), 1855-1859.

Schubert, S. D., and Coauthors, 2009: A U.S. CLIVAR project to assess and compare the responses of global climate models to drought-related SST forcing patterns: Overview and results. *J. Climate*, 22, 5251-5272.

Seager, R., Y. Kushnir, C. Herweijer, N. Naik, and J. Velez, 2005: Modeling of tropical forcing of persistent droughts and pluvials over western North America: 1856-2000. *J. Climate*, 18, 4065-4088.

Seager, R., R. Burgman, Y. Kushnir, A. Clement, E. Cook, N. Naik, and J. Miller, 2008: Tropical Pacific forcing of North American medieval megadroughts: Testing the concept with an atmosphere model forced by coral-reconstructed SSTs. *J. Climate*, 21, 6175-6190.

Seager, R., M. Ting, C. Li, N. Naik, B. Cook, J. Nakamura and H. Liu, 2013: Projections of

- declining surface-water availability for southwestern United States. *Nature Climatic Change*, 3, 482-486, doi:10.1038/nclimate1787.
- Seager, R. and M. Hoerling, 2014: Atmosphere and ocean origins of North American droughts. *J. Climate*, 27, 4581-4606.
- Seager, R., 2014: Decadal hydroclimate variability across the Americas. In *Climate Change, Multidecadal and Beyond*, World Scientific Series on Weather and Climate, in press.
- Sen Gupta, A., N. C. Jourdain, J. N. Brown, and D. Monselesan, 2013: Climate drift in the CMIP5 models. *J. Climate*, 26, 8597-8615.
- Sheffield, J., and Coauthors, 2013: North American Climate in CMIP5 Experiments. Part I: Evaluation of Historical Simulations of Continental and Regional Climatology. *J. Climate*, **26**, 9209–9245. doi: <http://dx.doi.org/10.1175/JCLI-D-12-00592.1>.
- Smerdon, J. E., B.I. Cook, E. R. Cook, and R. Seager, 2014: Bridging past and future climate across paleoclimatic reconstructions, observations, and models: A hydroclimate case study. *J. Clim.*, in review.
- Smith, T. M., and R. W. Reynolds, 2003: Extended reconstruction of global sea surface temperatures based on COADS data (1854–1997). *J. Climate*, 16, 1495–1510.
- Smith, D. M., A. A. Scaife, and B. Kirtman, 2012: What is the current state of scientific knowledge with regard to seasonal and decadal forecasting? *Environ. Res. Lett.*, 7, 015602, doi:10.1088/1748-9326/7/1/015602.
- St. George, S., D. M. Meko, and E. R. Cook, 2010: The seasonality of precipitation signals encoded within the North American Drought Atlas. *Holocene*, **20**, 983–988.

doi:[10.1177/0959683610365937](https://doi.org/10.1177/0959683610365937).

Sueyoshi, T., R. Ohgaito, A. Yamamoto, M. O. Chikamoto, T. Hajima, H. Okajima, M.

Yoshimori, M. Abe, R. O'ishi, F. Saito, S. Watanabe, M. Kawmiya, and A. Abe-Ouchi, (2013).
Set-up of the PMIP3 paleoclimate experiments conducted using an Earth system model,
MIROC-ESM. *Geoscientific Model Development*, 6(3), 819-836.

Taylor, K. E., R. J. Stouffer, and G. A. Meehl, 2012: An overview of CMIP5 and the experiment
design. *Bull. Amer. Meteorol. Soc.*, 93, 485-498.

Ting, M., Y. Kushnir, R. Seager, C. Li, 2009: Forced and Internal Twentieth-Century SST
Trends in the North Atlantic. *J. Climate*, 22, 1469–1481. doi:
<http://dx.doi.org/10.1175/2008JCLI2561.1>.

Ting, M., Y. Kushnir, R. Seager and C. Li, 2011: Robust Features of the Atlantic Multi-Decadal
Variability and its Climate Impacts. *Geophys. Res. Lett.*, L17705,
doi:10.1029/2011GL048712.

Vicente-Serrano, S. M., S. Beguería, and J. I. López-Moreno, 2010: A multiscalar drought
index sensitive to global warming: The standardized evapotranspiration index. *J.*
Climate, 23, 1696– 1718, doi:10.1175/2009JCLI2909.1.

Zhu, J., B. Huang, L. Marx, J. L. Kinter III, M. A. Balmaseda, R.-H. Zhang, and Z.-Z. Hu, 2012:
Ensemble ENSO hindcasts initialized from multiple ocean analyses. *Geophys. Res.*
Lett., 39, L09602, doi:[10.1029/2012GL051503](https://doi.org/10.1029/2012GL051503).

Modeling Center	Institute ID	Model Name
Beijing Climate Center, China Meteorological Administration	BCC	BCC-CSM1.1
National Center for Atmospheric Research	NCAR	CCSM4
NASA Goddard Institute for Space Studies	NASA GISS	GISS-E2-R
Institute Pierre-Simon Laplace	IPSL	IPSL-CM5A-LR
Japan Agency for Marine-Earth Science and Technology, Atmosphere and Ocean Research Institute (The University of Tokyo), and National Institute for Environmental Studies	MIROC	MIROC-ESM
Max-Planck-Intitut für Meteorologie (Max Planck Institute for Meteorology)	MPI-M	MPI-ESM-LR, MPI-ESM-P

Table 1: Model information for the analyzed CMIP5 simulations.

Figure Captions:

Figure 1: Correlations between gridpoint PDSI from the NADA or models and the DJF Niño3.4 index (top panels), the DJF Pacific Decadal Oscillation index (PDO-middle panel), and the JJA Atlantic Multidecadal Oscillation index (AMO-bottom panel). For the PDO and AMO, correlations are based on filtered (10-year LOWESS) PDSI and climate indices. The observed-reconstruction correlations (RECON) are from the overlapping period (1854-2005) between the NADA and the observed SST dataset [Smith and Reynolds, 2003] and the observed correlations (OBS) are from the 1950-2005 period in an observed PDSI dataset [Dai, 2004] and the same SST dataset. For the models, the teleconnection pattern was calculated for a sliding 152-year window (the length of the observed record). The plotted pattern is the 152-year segment with the teleconnection pattern that best matches the observed-reconstruction pattern as determined by the CPCS between the two fields. The middle panel shows the range in CPCS between the model pattern for each 152-year segment and the observed-reconstruction pattern. The bottom panel shows the range in the sum of squared correlation coefficients over North America for the model segments with the value from the observations and observation-to-reconstruction plotted as dashed grey and black lines, respectively.

Figure 2: (left panels) Correlation between the DJF Niño3.4 index and the DJF SST field for each model and the observed SST dataset. The autocorrelation of the Niño3.4 index for 1-6 year lags is plotted in the right panels with the red line indicating significance at the 95% level (two times the large-lag standard error). The plotted domain is 0°W-0°E, 40°S-40°N.

Figure 3: (left panels) The PDO pattern for each model and the observed SST dataset, calculated as the correlation between the DJF PDO index and the DJF SST field. The autocorrelation of the PDO index for 1-6 year lags is plotted in the right panels with the red line indicating significance at the 95% level (two times the large-lag standard error). These values are plotted for both the control (black) and forced (blue) simulations from each model. The plotted domain is 0°W-0°E, 20°S-70°N.

Figure 4: (left panels) Correlation between the JJA AMO index and the JJA SST field for each model and the observed SST dataset. The autocorrelation of the AMO index for 1-6 year lags is plotted in the right panels with the red line indicating significance at the 95% level (two times the large-lag standard error). These values are plotted for both the control (black) and forced (blue) simulations from each model. The plotted domain is 180°W-180°E, 20°S-70°N.

Figure 5: (top panel) The range in the CPCS between the simulated ENSO, PDO and AMO spatial patterns calculated for a sliding 125-year window (length of the observed SST dataset) across the full model simulations and the observed spatial patterns. The observed target patterns are plotted in the bottom panel. The plotted domain is 0°W-0°E, 30°S-80°N. The boxes over which the CPCS values were calculated for each region are designated by the black dashed lines.

Figure 6: The variance of the Niño3.4 index (left panel), percent variance explained in Pacific SSTs by the PDO mode of variability (middle panel), and variance of the 10-year low pass filtered AMO index (right panel). These were computed for each full control run and for the observed dataset over the period 1854-2005 C.E.

Figure 7: Drought recurrence intervals for each region. Reconstruction results are shown in black. Model results are shown in color, where the lighter shaded bars of the paired colors represent the recurrence value for a control simulation from each model, while the darker shaded bars are from the associated forced simulation.

Figure 8: Drought recurrence intervals for each type of pan-continental drought. Reconstruction results are shown in black. Model results are shown in color, where the lighter shaded bars of the paired colors represent the recurrence value for a control simulation from each model, while the darker shaded bars are from the associated forced simulation. To maintain consistency with Cook et al. [2014], drought years were allowed to overlap between the three- and four-region droughts.

Figure 9: (top five rows) PDSI composite or average over all pan-continental drought years ($PDSI \leq -0.5$) of each type. The bottom panel is the range in CPCS for individual droughts with the NADA composite pattern. Boxplot color indicates the associated control model simulation or reconstruction. Unlike in previous figures, drought years were not allowed to overlap between the three- and four-region droughts.

Figure 10: Number of pan-continental drought years ($PDSI \leq -0.5$) in each century relative to the mean number of droughts per century between 1000-2000 C.E., calculated for all possible types of pan-continental drought. To maintain consistency with Cook et al. [2014], drought years were allowed to overlap between the three- and four-region drought categories. Bar color indicates the associated forced model simulation or reconstruction.

Figure 11: Ranges in the number of drought years ($PDSI \leq -0.5$) for each pan-continental drought type. This was calculated for a sliding 100-year window across the model record

or reconstruction. Box plot color indicates the associated forced model simulation or reconstruction.

Figure 12: Mean values of climate indices during pan-continental drought years ($PDSI \leq -0.5$) for the full control simulations and the overlapping period between the observed SST dataset and the NADA (1854-2005 C.E.). The top panel is the Niño3.4 index, the middle panel is the PDO index, and the bottom panel is the AMO index. Significance at the 90% level is indicated by an asterisk and was calculated using the resampling test described in Section 2c. Unlike in previous figures, drought years were not allowed to overlap between the three- and four-region droughts.

Figure 13: The observed DJF Niño3.4, DJF PDO and JJA AMO indices for the period 1854-2005 C.E. are plotted as solid black lines in the left panels. For the PDO and AMO the filled regions (red for positive, blue for negative) are the smoothed time-series using a ten-year LOWESS spline, while for the Niño3.4 index the filled regions are the unfiltered interannual data. The timing of each pan-continental drought occurrence is indicated with a grey bar (all five types of pan-continental drought are considered together). The right panel plots the posterior distribution of the frequency of pan-continental drought occurrence (all types considered together) for the full data (black) and for the subset of data with a positive AMO (red), negative PDO (blue), or negative Niño3.4 (green) index and years with combinations of two or all three of these conditions. The distributions for combinations of two conditions are dashed using the two respective colors while the distribution for the combination of all three conditions is plotted in purple. The distributions were computed using a Bayesian

framework with an uninformative prior and pan-continental drought occurrence treated as a Bernoulli process.

Figure 14: The posterior distributions for each model of the frequency of pan-continental drought occurrence (all types considered together) for the full data (black) and for the subset of data with a positive AMO (red), negative PDO (blue), or negative Niño3.4 (green) index and years with combinations of two or all three of these conditions. The distributions for combinations of two conditions are dashed using the two respective colors while the distribution for the combination of all three conditions is plotted in purple. The distributions were computed using a Bayesian framework with an uninformative prior and pan-continental drought occurrence treated as a Bernoulli process.

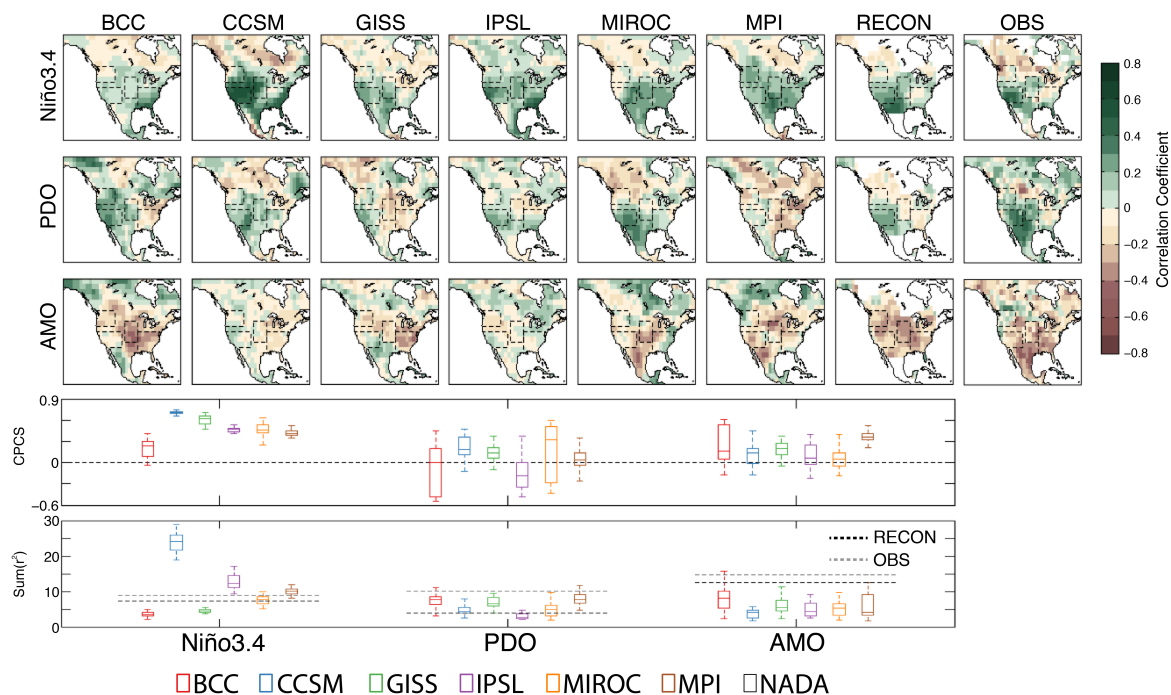


Figure 1: Correlations between gridpoint PDSI from the NADA or models and the DJF Niño3.4 index (top panels), the DJF Pacific Decadal Oscillation index (PDO-middle panel), and the JJA Atlantic Multidecadal Oscillation index (AMO-bottom panel). For the PDO and AMO, correlations are based on filtered (10-year LOWESS) PDSI and climate indices. The observed-reconstruction correlations (RECON) are from the overlapping period (1854-2005) between the NADA and the observed SST dataset [Smith and Reynolds, 2003] and the observed correlations (OBS) are from the 1950-2005 period in an observed PDSI dataset [Dai, 2004] and the same SST dataset. For the models, the teleconnection pattern was calculated for a sliding 152-year window (the length of the observed record). The plotted pattern is the 152-year segment with the teleconnection pattern that best matches the observed-reconstruction pattern as determined by the CPCS between the two fields. The middle panel shows the range in CPCS between the model pattern for each 152-year segment and the observed-reconstruction pattern. The bottom panel shows the range in the sum of squared correlation coefficients over North America for the model segments with the value from the observations and observation-to-reconstruction plotted as dashed grey and black lines, respectively.

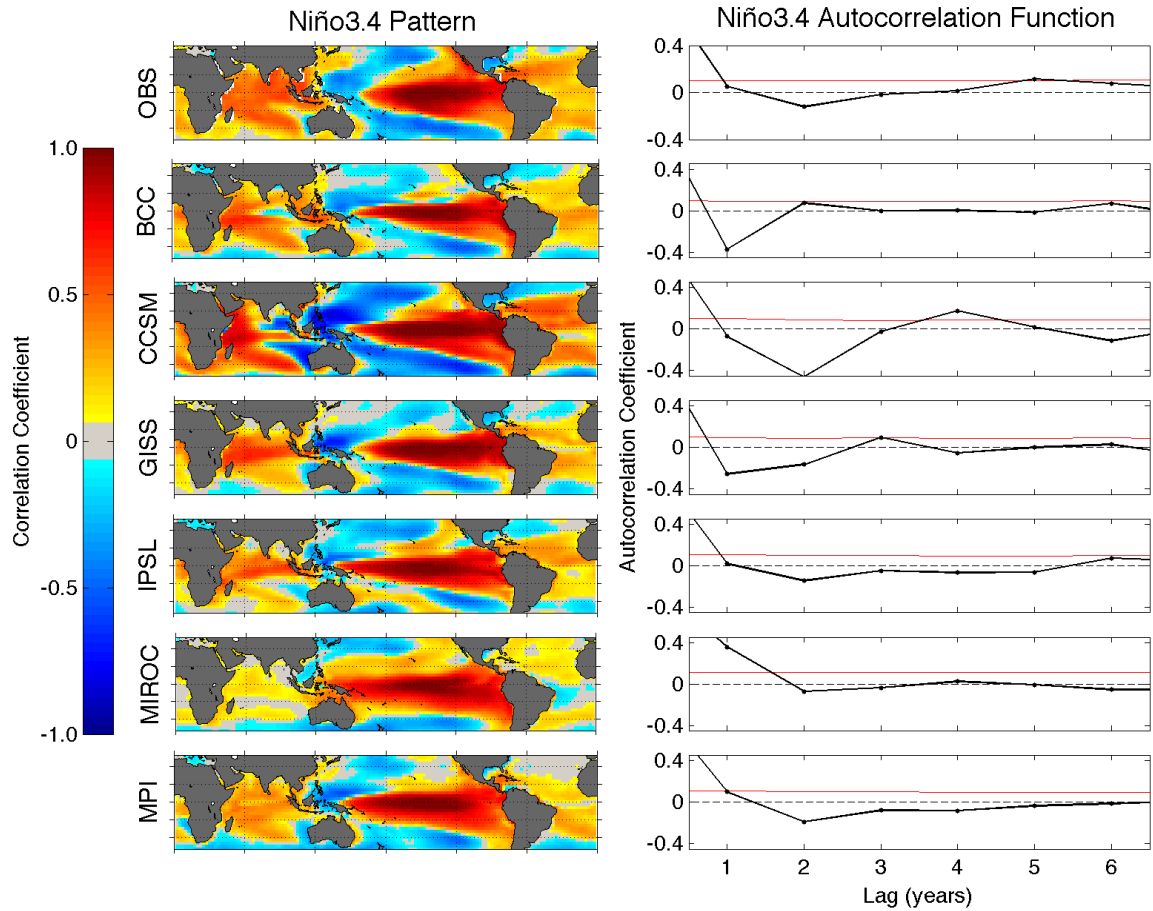


Figure 2: (left panels) Correlation between the DJF Niño3.4 index and the DJF SST field for each model and the observed SST dataset. The autocorrelation of the Niño3.4 index for 1-6 year lags is plotted in the right panels with the red line indicating significance at the 95% level (two times the large-lag standard error). The plotted domain is 0°W-0°E, 40°S-40°N.

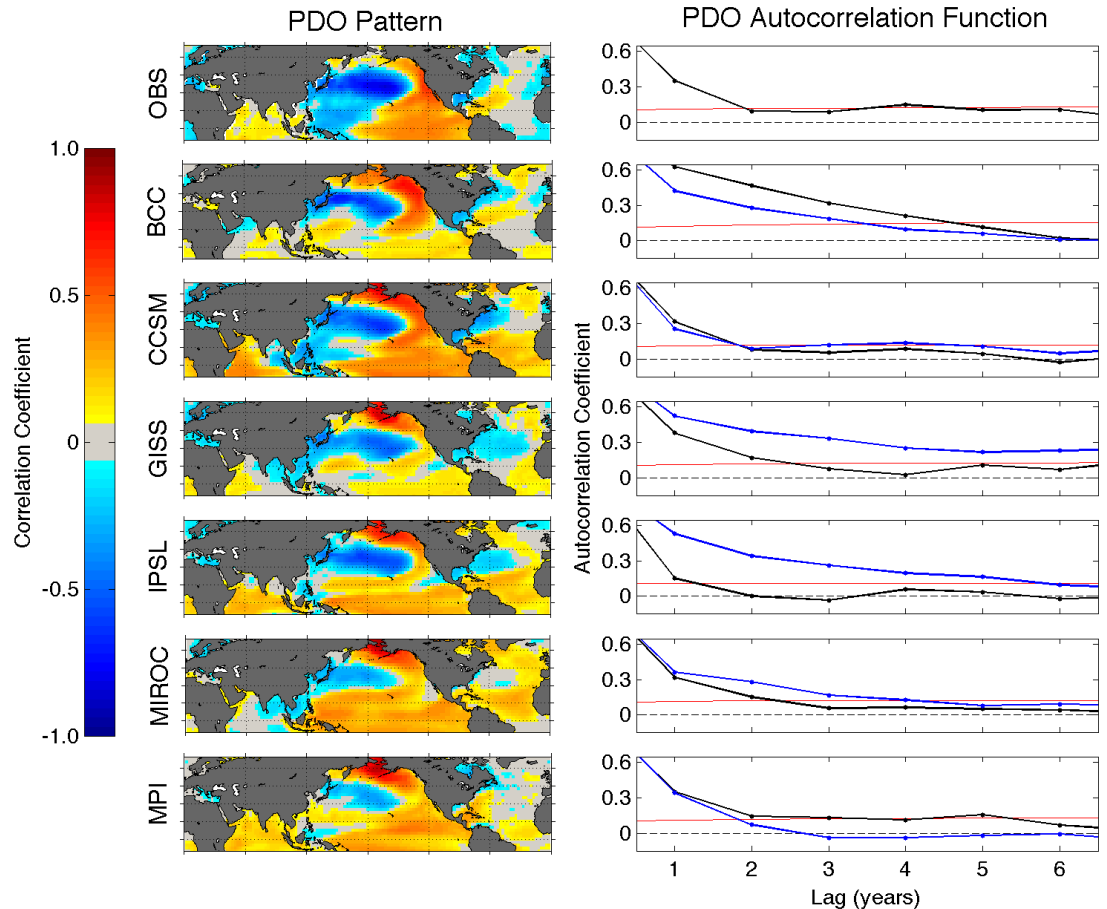


Figure 3: (left panels) The PDO pattern for each model and the observed SST dataset, calculated as the correlation between the DJF PDO index and the DJF SST field. The autocorrelation of the PDO index for 1-6 year lags is plotted in the right panels with the red line indicating significance at the 95% level (two times the large-lag standard error). These values are plotted for both the control (black) and forced (blue) simulations from each model. The plotted domain is 0°W-0°E, 20°S-70°N.

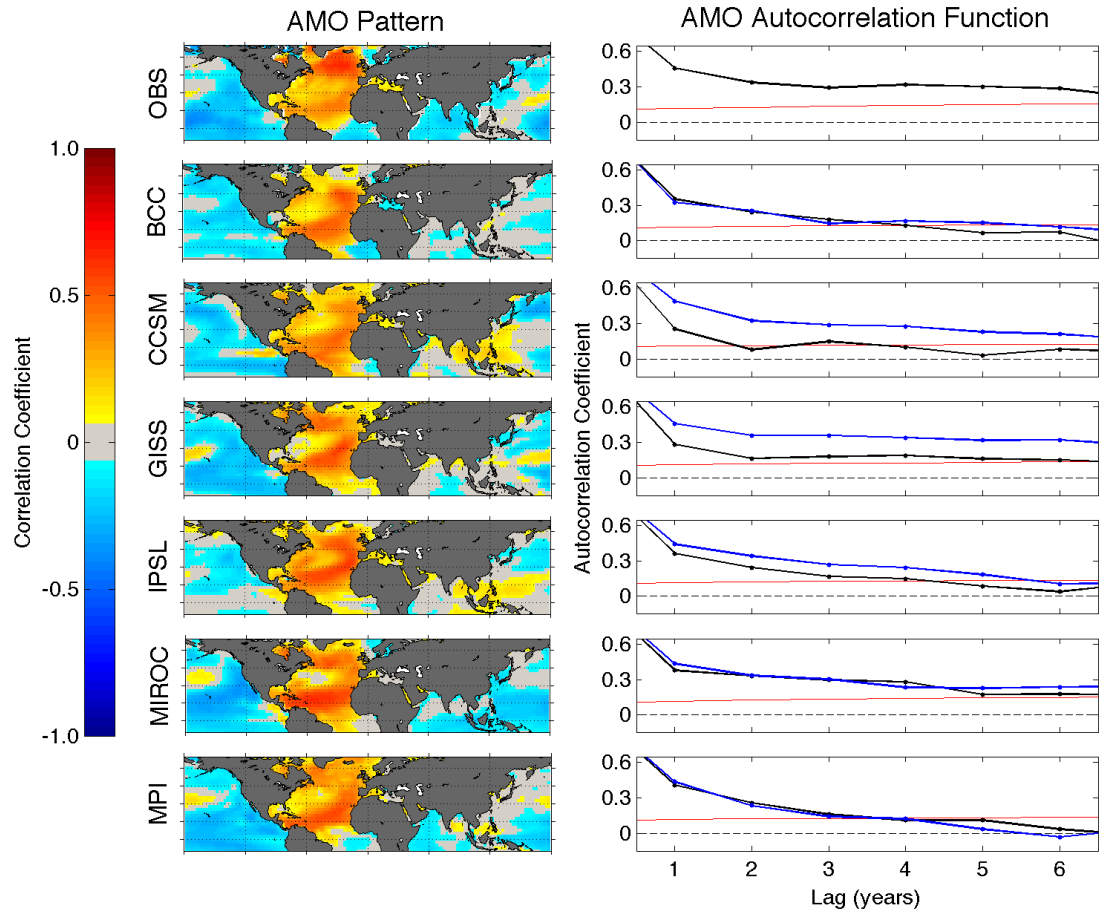


Figure 4: (left panels) Correlation between the JJA AMO index and the JJA SST field for each model and the observed SST dataset. The autocorrelation of the AMO index for 1-6 year lags is plotted in the right panels with the red line indicating significance at the 95% level (two times the large-lag standard error). These values are plotted for both the control (black) and forced (blue) simulations from each model. The plotted domain is 180°W-180°E, 20°S-70°N.

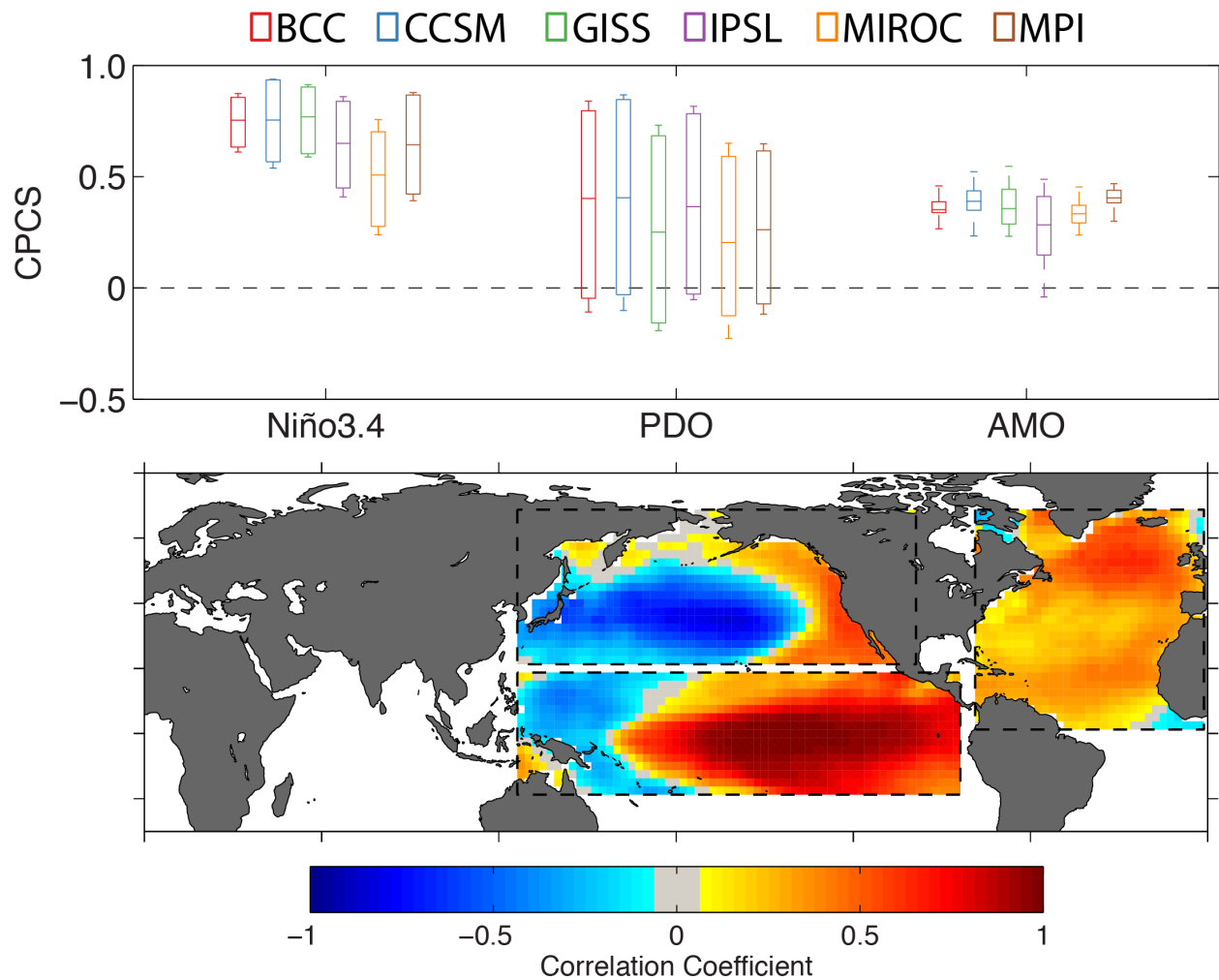


Figure 5: (top panel) The range in the CPCS between the simulated ENSO, PDO and AMO spatial patterns calculated for a sliding 125-year window (length of the observed SST dataset) across the full model simulations and the observed spatial patterns. The observed target patterns are plotted in the bottom panel. The plotted domain is 0°W-0°E, 30°S-80°N. The boxes over which the CPCS values were calculated for each region are designated by the black dashed lines.

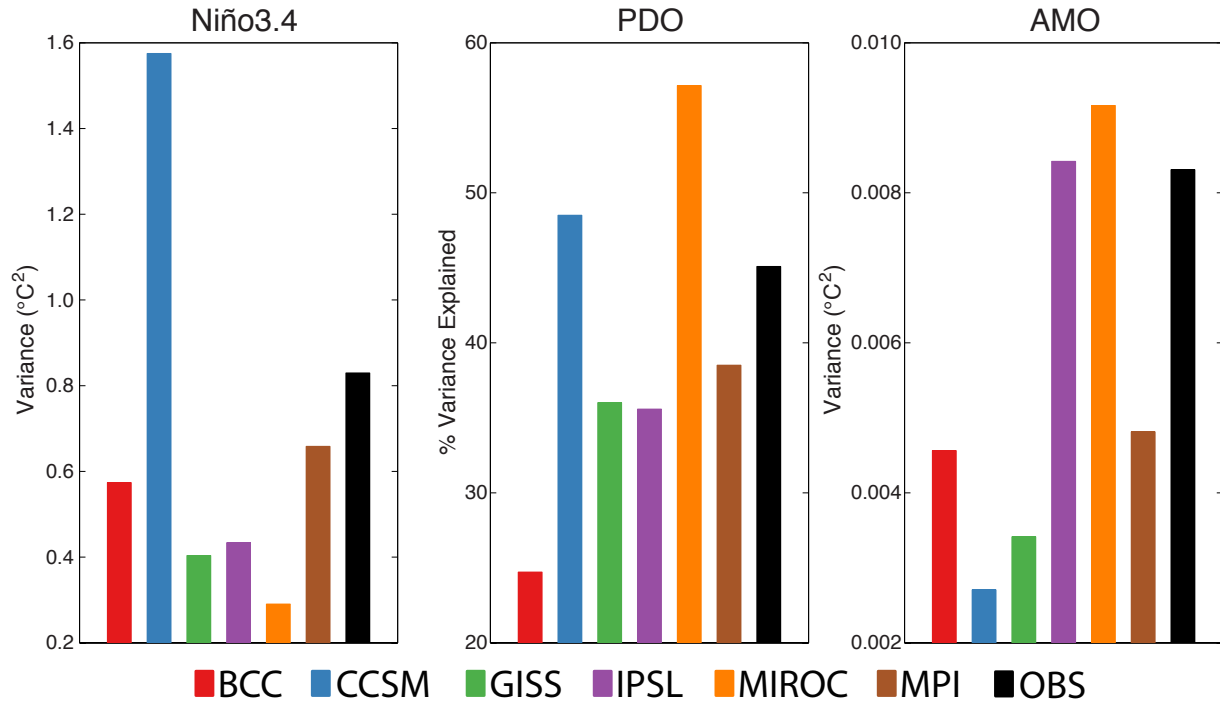


Figure 6: The variance of the Niño3.4 index (left panel), percent variance explained in Pacific SSTs by the PDO mode of variability (middle panel), and variance of the 10-year low pass filtered AMO index (right panel). These were computed for each full control run and for the observed dataset over the period 1854-2005 C.E.

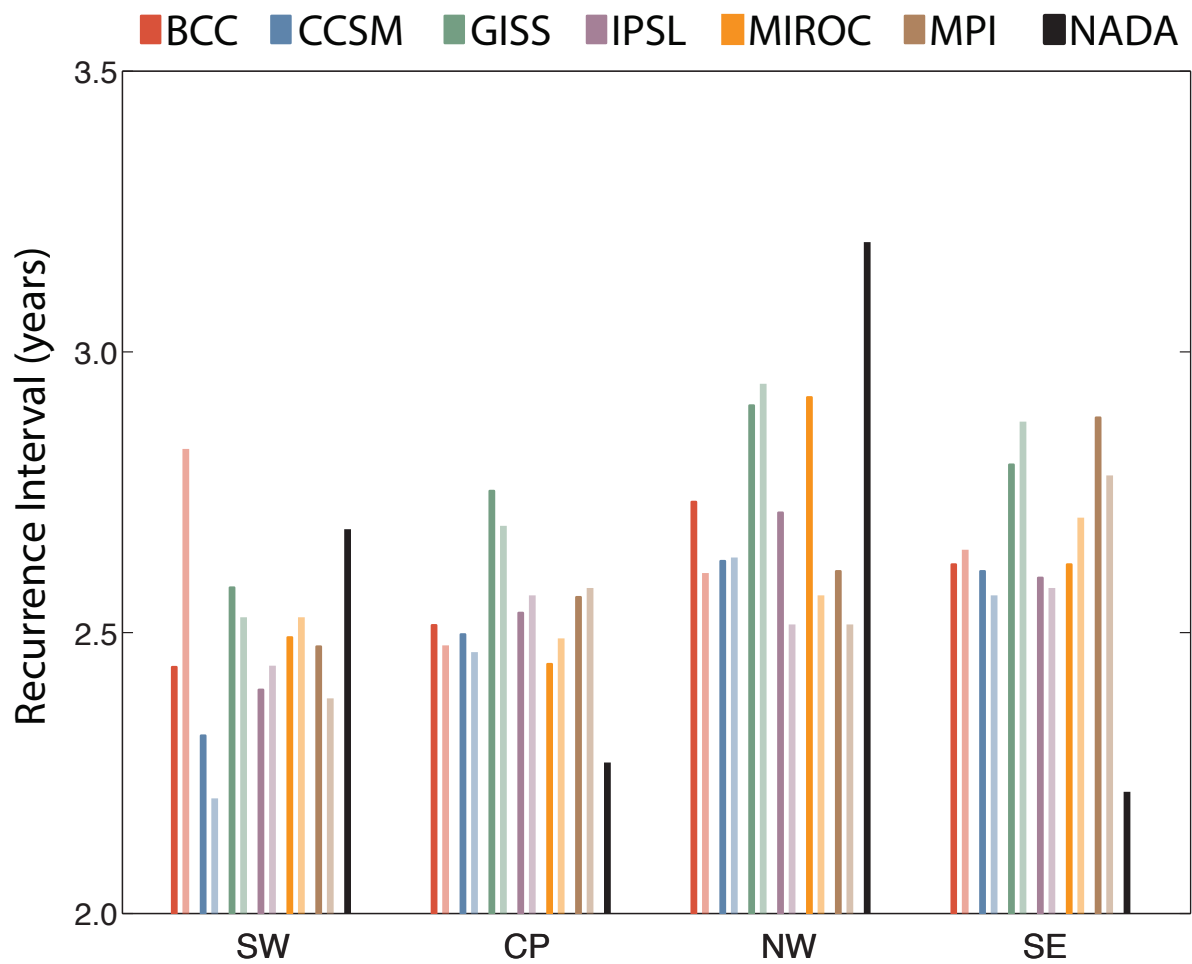


Figure 7: Drought recurrence intervals for each region. Reconstruction results are shown in black. Model results are shown in color, where the lighter shaded bars of the paired colors represent the recurrence value for a control simulation from each model, while the darker shaded bars are from the associated forced simulation.

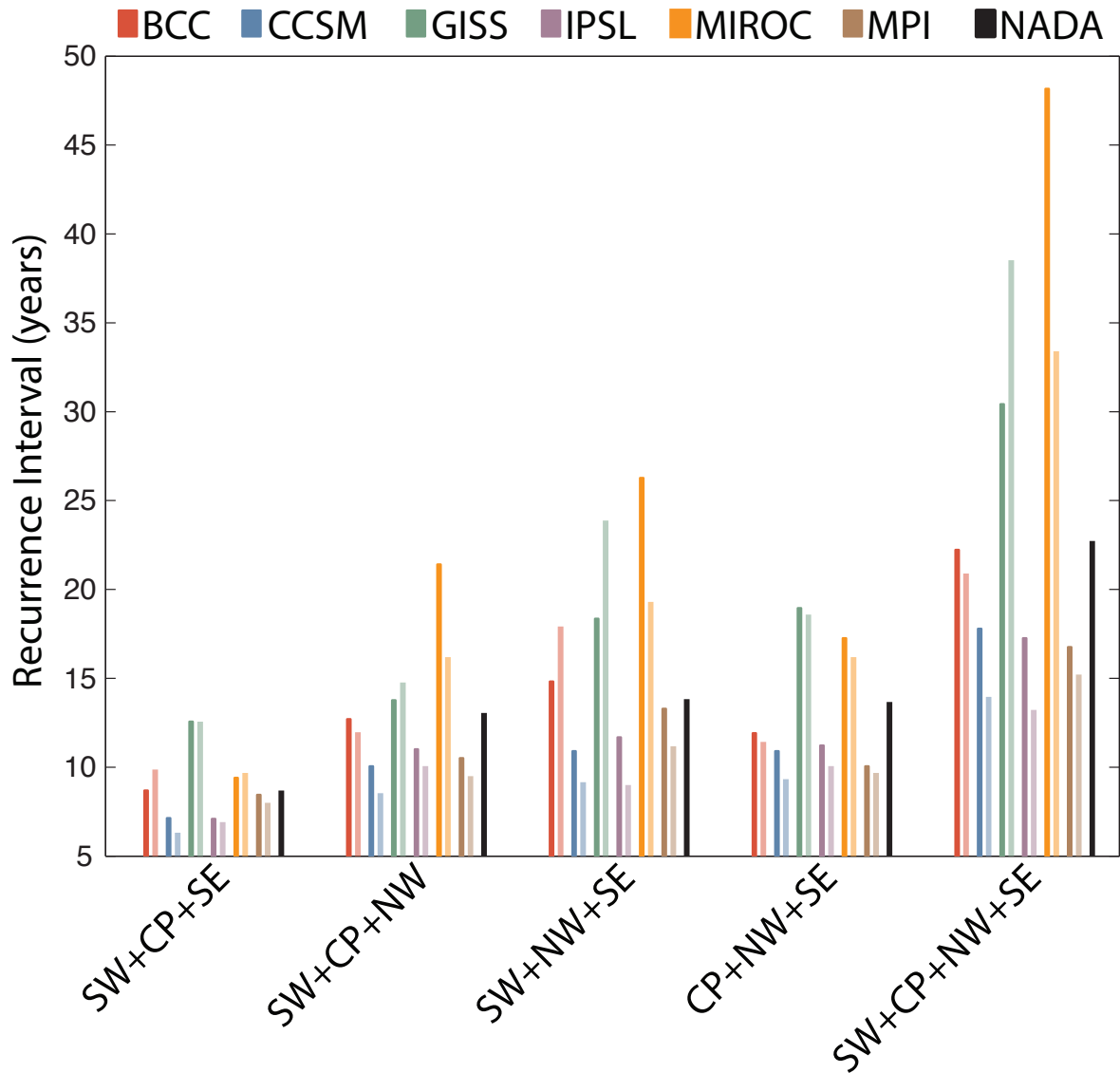


Figure 8: Drought recurrence intervals for each type of pan-continental drought. Reconstruction results are shown in black. Model results are shown in color, where the lighter shaded bars of the paired colors represent the recurrence value for a control simulation from each model, while the darker shaded bars are from the associated forced simulation. To maintain consistency with Cook et al. [2014], drought years were allowed to overlap between the three- and four-region droughts.

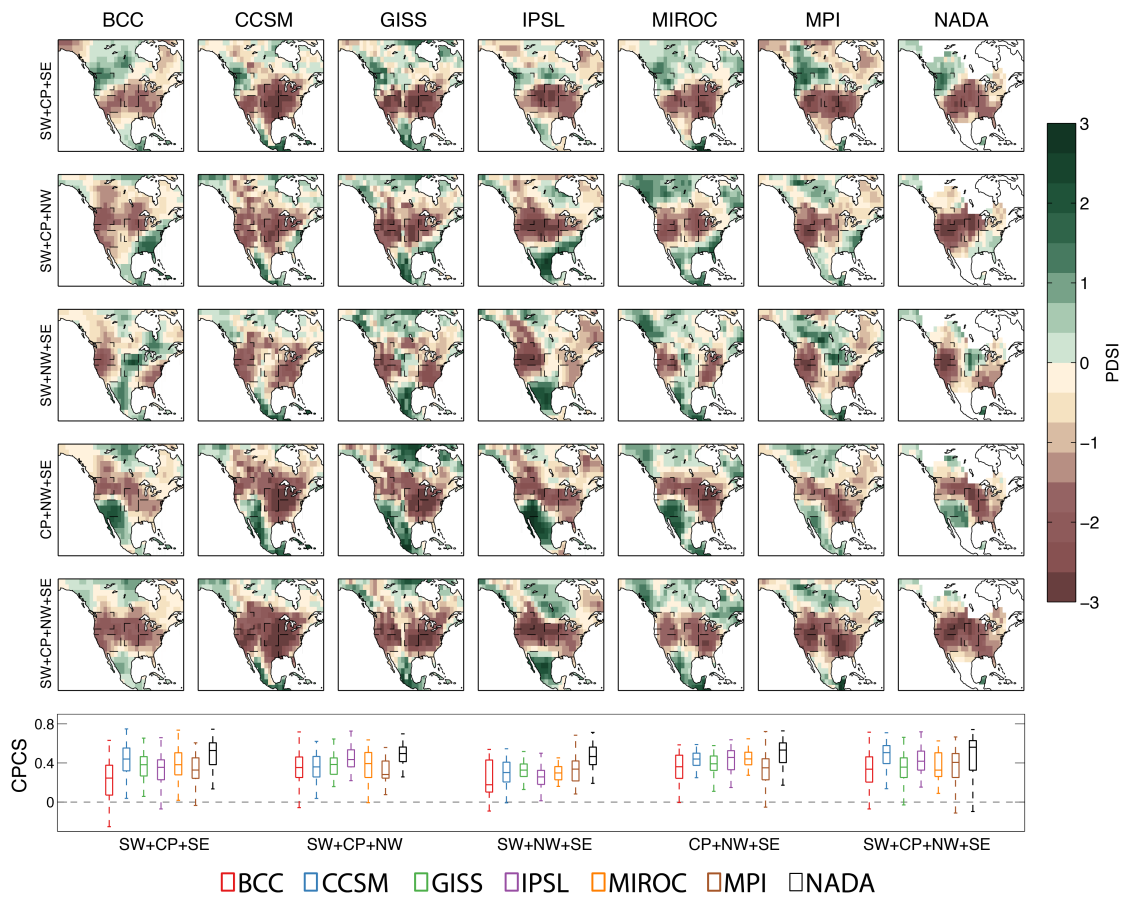


Figure 9: (top five rows) PDSI composite or average over all pan-continental drought years ($PDSI \leq -0.5$) of each type. The bottom panel is the range in CPCS for individual droughts with the NADA composite pattern. Boxplot color indicates the associated control model simulation or reconstruction. Unlike in previous figures, drought years were not allowed to overlap between the three- and four-region droughts.

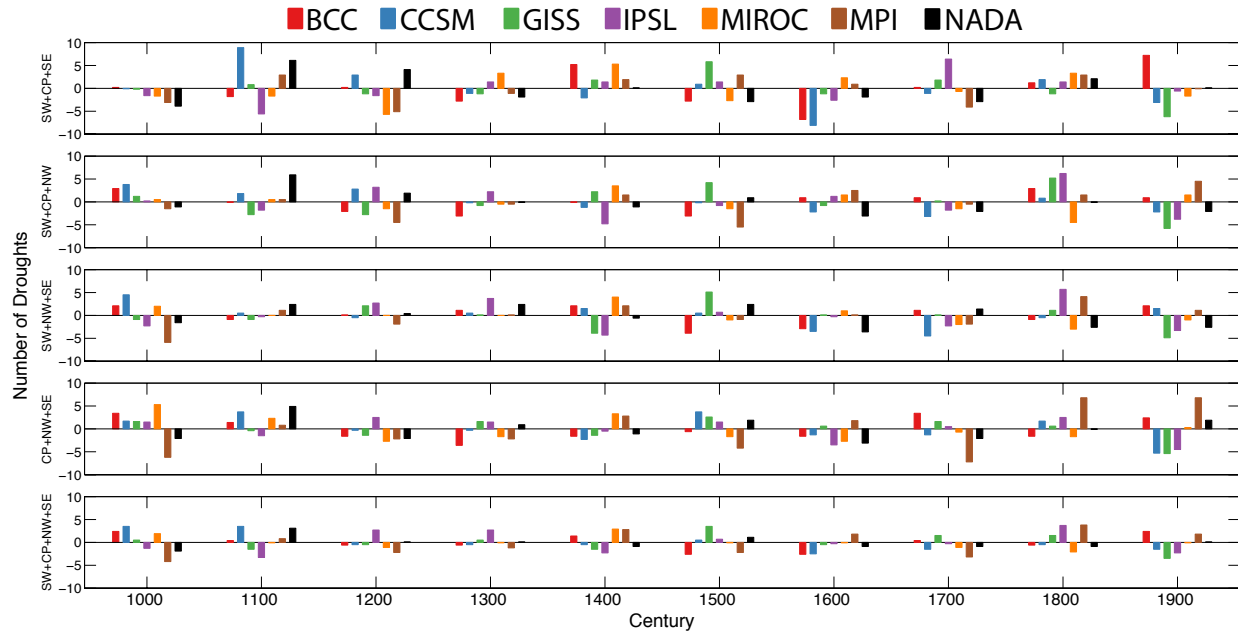


Figure 10: Number of pan-continental drought years ($PDSI \leq -0.5$) in each century relative to the mean number of droughts per century between 1000-2000 C.E., calculated for all possible types of pan-continental drought. To maintain consistency with Cook et al. [2014], drought years were allowed to overlap between the three- and four-region drought categories. Bar color indicates the associated forced model simulation or reconstruction.

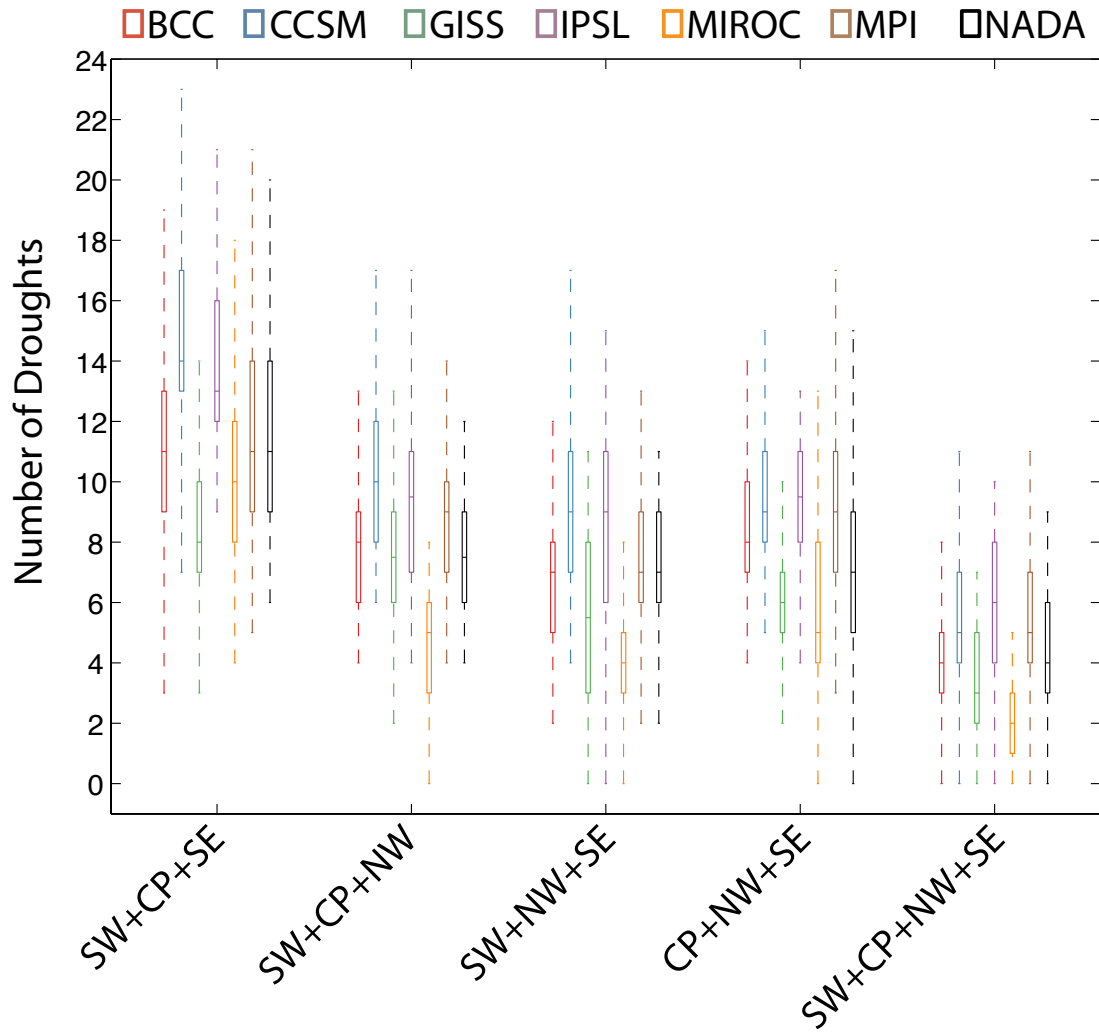


Figure 11: Ranges in the number of drought years ($PDSI \leq -0.5$) for each pan-continent drought type. This was calculated for a sliding 100-year window across the model record or reconstruction. Box plot color indicates the associated forced model simulation or reconstruction.

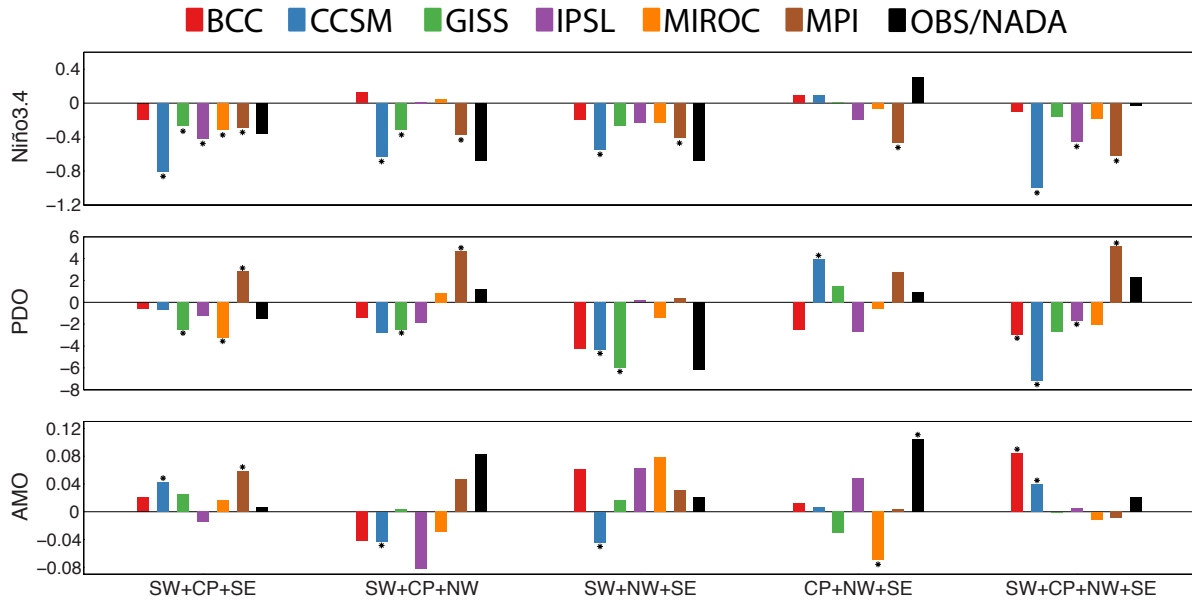


Figure 12: Mean values of climate indices during pan-continental drought years ($PDSI \leq -0.5$) for the full control simulations and the overlapping period between the observed SST dataset and the NADA (1854-2005 C.E.). The top panel is the Niño3.4 index, the middle panel is the PDO index, and the bottom panel is the AMO index. Significance at the 90% level is indicated by an asterisk and was calculated using the resampling test described in Section 2c. Unlike in previous figures, drought years were not allowed to overlap between the three- and four-region droughts.

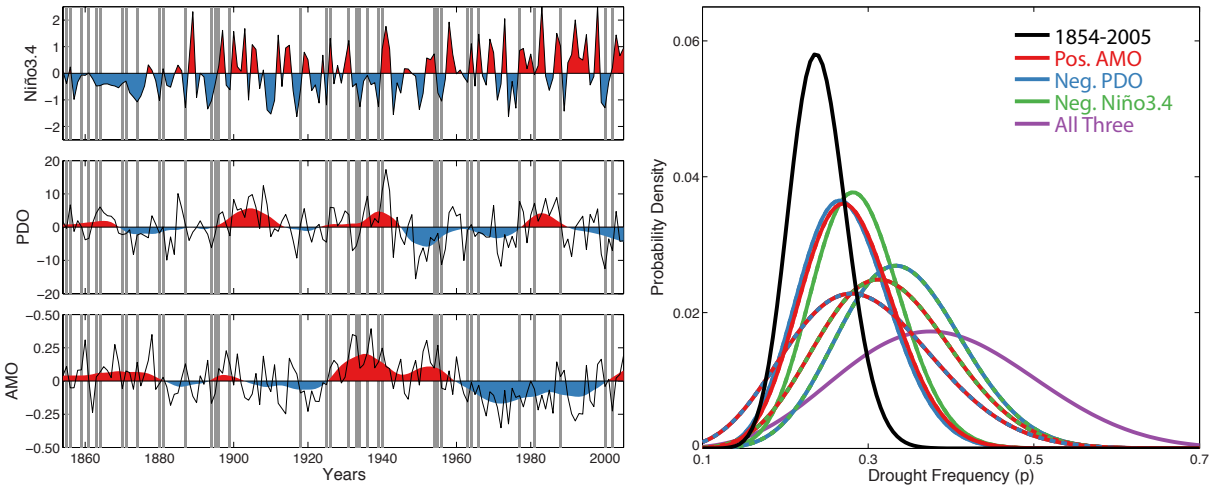


Figure 13: The observed DJF Niño3.4, DJF PDO and JJA AMO indices for the period 1854-2005 C.E. are plotted as solid black lines in the left panels. For the PDO and AMO the filled regions (red for positive, blue for negative) are the smoothed time-series using a ten-year LOWESS spline, while for the Niño3.4 index the filled regions are the unfiltered interannual data. The timing of each pan-continental drought occurrence is indicated with a grey bar (all five types of pan-continental drought are considered together). The right panel plots the posterior distribution of the frequency of pan-continental drought occurrence (all types considered together) for the full data (black) and for the subset of data with a positive AMO (red), negative PDO (blue), or negative Niño3.4 (green) index and years with combinations of two or all three of these conditions. The distributions for combinations of two conditions are dashed using the two respective colors while the distribution for the combination of all three conditions is plotted in purple. The distributions were computed using a Bayesian framework with an uninformative prior and pan-continental drought occurrence treated as a Bernoulli process.

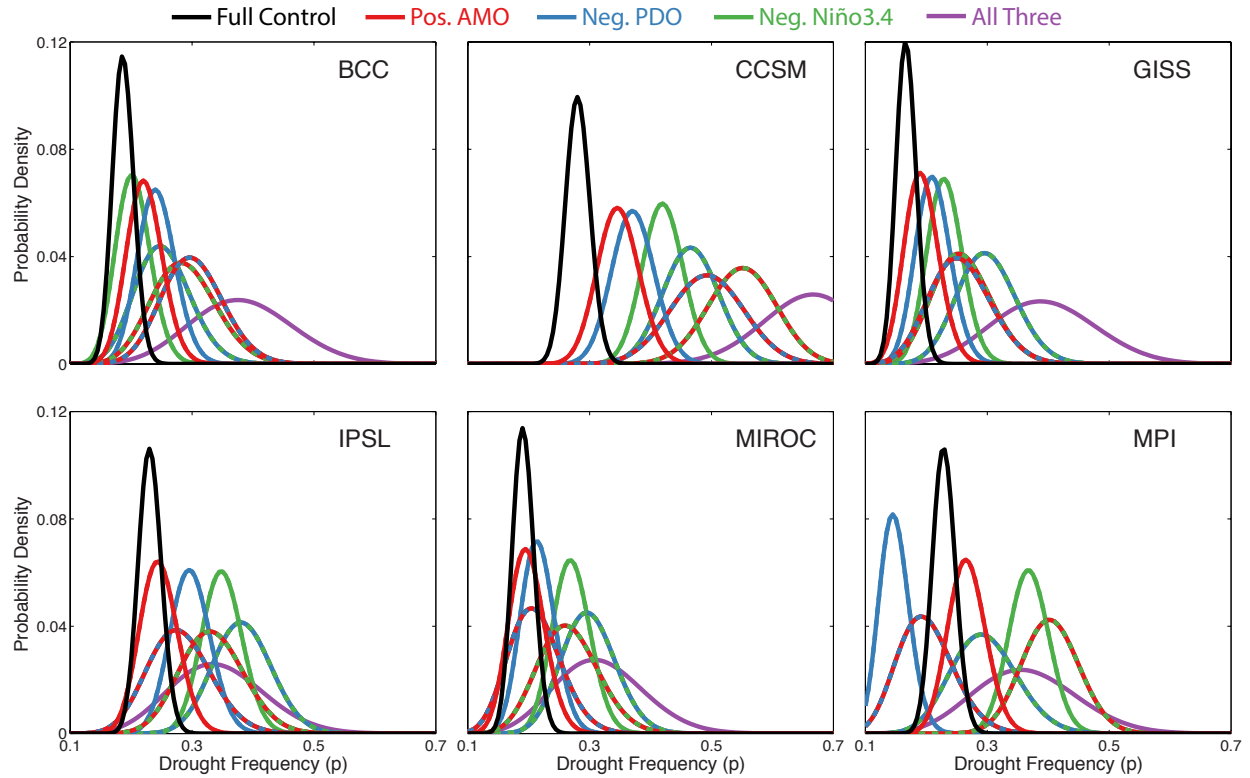


Figure 14: The posterior distributions for each model of the frequency of pan-continental drought occurrence (all types considered together) for the full data (black) and for the subset of data with a positive AMO (red), negative PDO (blue), or negative Niño3.4 (green) index and years with combinations of two or all three of these conditions. The distributions for combinations of two conditions are dashed using the two respective colors while the distribution for the combination of all three conditions is plotted in purple. The distributions were computed using a Bayesian framework with an uninformative prior and pan-continental drought occurrence treated as a Bernoulli process.